

Electronic Theses and Dissertations, 2004-2019

2013

Experimental And Numerical Investigation Of Aerodynamic Unsteadiness In A Gas Turbine Midframe

Matthew Golsen
University of Central Florida

 Part of the [Mechanical Engineering Commons](#)
Find similar works at: <https://stars.library.ucf.edu/etd>
University of Central Florida Libraries <http://library.ucf.edu>

This Masters Thesis (Open Access) is brought to you for free and open access by STARS. It has been accepted for inclusion in Electronic Theses and Dissertations, 2004-2019 by an authorized administrator of STARS. For more information, please contact STARS@ucf.edu.

STARS Citation

Golsen, Matthew, "Experimental And Numerical Investigation Of Aerodynamic Unsteadiness In A Gas Turbine Midframe" (2013). *Electronic Theses and Dissertations, 2004-2019*. 2632.
<https://stars.library.ucf.edu/etd/2632>

EXPERIMENTAL AND NUMERICAL INVESTIGATION OF
AERODYNAMIC UNSTEADINESS IN A GAS TURBINE MIDFRAME

by

MATTHEW J. GOLSEN
B.S. University of Central Florida 2011

A thesis submitted in partial fulfillment of the requirements
for the degree of Master of Science
in the Department of Mechanical, Materials, and Aerospace Engineering
in the College of Engineering and Computer Science
at the University of Central Florida
Orlando, Florida

Summer Term
2013

© 2013 Matthew J. Golsen

ABSTRACT

As modern gas turbines implement more and more complex geometry to increase life and efficiency, attention to unsteady aerodynamic behavior becomes more important. Computational optimization schemes are contributing to advanced geometries in order to reduce aerodynamic losses and increase the life of components. These advanced geometries are less representative of cylinder and backward facing steps which have been used as analogous geometries for most aerodynamic unsteadiness research. One region which contains a high degree of flow unsteadiness and a direct influence on engine performance is that of the MidFrame.

The MidFrame (or combustor-diffuser system) is the region encompassing the main gas path from the exit of the compressor to the inlet of the first stage turbine. This region contains myriad flow scenarios including diffusion, bluff bodies, direct impingement, high degree of streamline curvature, separated flow, and recirculation. This represents the most complex and diverse flow field in the entire engine. The role of the MidFrame is to redirect the flow from the compressor into the combustion system with minimal pressure loss while supplying high pressure air to the secondary air system. Various casing geometries, compressor exit diffuser shapes, and flow conditioning equipment have been tested to reduce pressure loss and increase uniformity entering the combustors.

Much of the current research in this area focuses on aero propulsion geometries with annular combustors or scaled models of the power generation geometries. Due to the complexity and size of the domain accessibility with physical probe measurements becomes challenging. The current work uses additional measurement techniques to measure flow unsteadiness in the domain. The methodology for identifying and quantifying the sources of unsteadiness are

developed herein. Sensitivity of MidFrame unsteadiness to compressor exit conditions is shown for three different velocity profiles. The result is an extensive database of measurements which can serve as a benchmark for radical new designs to ensure that the unsteadiness levels do not supersede previous successful levels.

To my parents for instilling in me insatiable drive.

To my girlfriend for remaining through all of the sleepless nights.

To my colleagues at CATER for inspiring and offering opportunity.

ACKNOWLEDGMENTS

I express my gratitude to my committee members for lending their time to my work. Extra thanks to Dr. Mark Ricklick, Bryan Bernier, and Greg Natsui for lending their experience to guide me through the most demanding times. Special thanks to my thesis chair, Dr. Jay Kapat, for inspiring accountability and granting opportunities abound. I would like to thank Dr. Jose Rodriguez for granting me the opportunity to apply what I've learned to the latest design technologies.

This work was completed using equipment funded by Siemens Energy Inc.

TABLE OF CONTENTS

LIST OF FIGURES	viii
LIST OF TABLES	x
NOMENCLATURE	xi
INTRODUCTION	1
Power Production and Propulsion.....	1
Flow Management	3
The MidFrame	5
EXISTING WORK.....	10
MOTIVATION.....	13
EXPERIMENTAL PROCEDURE	14
Steady Instrumentation	14
Unsteady Instrumentation.....	24
NUMERICAL SETUP.....	31
RESULTS	34
Experimental Results	34
Steady Numerical Results.....	67
CONCLUSIONS.....	73
APPENDIX: DETAILED UNCERTAINTY CALCULATIONS	75
REFERENCES	79

LIST OF FIGURES

Figure 1: Brayton Cycle and the deviation from ideal performance.....	2
Figure 2: Example of the coolant flow and MidFrame location on a GE gas turbine	5
Figure 3: Difference between aero and power gen MidFrame geometries	6
Figure 4: Flow pattern of land based MidFrame.....	9
Figure 5: Streamlines through the exhaust diffuser and plenum chamber	15
Figure 6: Location of flow conditioning screens relative to the velocity profile screens	15
Figure 7: Rendering of the dual support small diameter Pitot-static probe traverse.....	16
Figure 8: Flow schematic of the main MidFrame.....	19
Figure 9: CED bottom wall static pressure taps.....	19
Figure 10: CED sidewall and CED exit region static pressure tap locations.....	21
Figure 11: Location of two of four rows of static pressure taps in the combustor portal	21
Figure 12: Cross section of Kiel probe measurement planes (left) and image of instrumented combustor portal (right).....	22
Figure 13: Inlet area average and transition exit single point velocity correlation	23
Figure 14: Transition exit velocity profiles and single point measurement for correlation denoted	23
Figure 15: Schematic of unsteady instrumentation validation experiment	27
Figure 16: Results of unsteady instrumentation validation experiment.....	28
Figure 17: Influence of bin size on spectral averaging	29
Figure 18: Ten raw overlaid signals (blue) with resulting clean signal using spectral and arithmetic averaging (red).....	30
Figure 19: Centerline cross section of mesh	32
Figure 20: Simplified inlet profiles mapped from experimental cases	33
Figure 21: Overview of boundary conditions	33
Figure 22: FA (top) and SB (bottom) inlet configurations and inlet velocity contours	35
Figure 23: Microtuft visualization on bottom wall for the FA (top) and SB (bottom) cases.....	35
Figure 24: Turbulence intensity of CED inlet in radial direction for $\theta = 0^\circ$	36
Figure 25: CED C_p curves using bottom wall static pressure measurements.....	38
Figure 26: Sidewall C_p measurements at exit of CED	38
Figure 27: Combustor portal total pressure variation at $z/L = 0.55$	39
Figure 28: Circumferential and axial pressure coefficient in the combustor portal.....	40
Figure 29: Microphone and mic-accel coherence for CED location SB case	42
Figure 30: Microphone and mic-accel coherence signal for CED location FA case	43
Figure 31: Microphone and mic-accel coherence signal for BDC location SB case	45
Figure 32: Microphone and mic-accel coherence signal for BDC location FA case	46
Figure 33: Microphone and mic-accel coherence signal for TDC location SB case	47
Figure 34: Microphone and mic-accel coherence signal for TDC location FA case	48
Figure 35: Microphone and mic-accel coherence signal for transition location SB case	50
Figure 36: Microphone and mic-accel coherence signal for transition location FA case	51
Figure 37: Microphone and mic-accel coherence signal for top hat location SB case	52
Figure 38: Microphone and mic-accel coherence signal for top hat location FA case	53
Figure 39: Coherence between CED and other microphone locations for SB case.....	55
Figure 40: Coherence between CED and other microphone locations for FA case.....	56
Figure 41: Coherence between BDC and other microphone locations for SB case.....	57
Figure 42: Coherence between BDC and other microphone locations for FA case	58

Figure 43: Coherence between TDC and other microphone locations for SB case	59
Figure 44: Coherence between TDC and other microphone locations for FA case.....	60
Figure 45: Coherence between transition and other microphone locations for SB case.....	61
Figure 46: Coherence between transition and other microphone locations for FA case.....	62
Figure 47: Coherence between top hat and other microphone locations for SB case.....	63
Figure 48: Coherence between top hat and other microphone locations for FA case.....	64
Figure 49: FFT for backward facing step shear layer FA case	65
Figure 50: FFT for the c-stage cylinder for the FA case.....	66
Figure 51: Comparison between centerline mean flow for the two inlet conditions	68
Figure 52: Comparison between near wall flow for the two inlet cases	69
Figure 53: Cp Plot comparison with experimental and CFD predictions	70
Figure 54: Comparison of top hat region total pressure profiles for CFD cases.....	71
Figure 55: Comparison of top hat region axial profiles for CFD cases	71
Figure 56: Total Pressure loss coefficient comparison	72

LIST OF TABLES

Table 1: Summary of inlet conditions.....	18
Table 2: Summary of screen characteristics	18
Table 3: Summary of CFD cases	72

LIST OF NOMENCLATURE

A	Area
c_p	Specific heat at constant pressure
Cp	Static pressure coefficient
L	Length
m	Mass flow rate
RIT	Rotor inlet temperature
r	Radial distance from machine axis
Re	Reynolds number
S	Strouhal number
T	Temperature
Tu	Turbulence intensity
U	Velocity
u'	Streamwise velocity fluctuation
x	streamwise distance
Greek	
δ	Disturbance layer thickness
η	Efficiency
k	Ratio of specific heats (c_p/c_v)
ρ	Density
θ	Circumferential angle

Subscripts

∞ Mainstream

INTRODUCTION

Power Production and Propulsion

The heat engine represents one of the greatest achievements of man as it allows the useful production of work above and beyond what would be capable even beyond an entire population of willing hands. The genesis of utilizing energy sources for useful work dates back millennia with wind and water power. These resources are intermittent and mostly uncontrollable. The chemical reaction of combustion allowed the release of energy on command and when directed through an engine, allows high work output when and where it is required. One of the most prolific examples of such a heat engine is the gas turbine.

The gas turbine follows the Brayton cycle with the compression, combustion, and expansion stages are occurring simultaneously and disjointed spatially. The gas turbine offers many advantages over the reciprocating internal combustion engine. These include high power to weight ratio, reduced vibration, fuel versatility, and high potential for waste heat recovery. As a result these engines find wide application from aero propulsion to industrial and chemical process power generation. Since the introduction of gas turbines in the 1930's much research has gone into how to increase the efficiency and reliability of the technology. The Brayton cycle T-s diagram shown in Figure 1 can illustrate the impact of the operating temperature and pressure on the work output. (Cengel and Boles 2006) The thermal efficiency of the cycle can be written as in Equation 1. While T_1 is fixed by atmospheric conditions and T_2 is a result of the compression stage, T_3 can be directly controlled via the fuel air ratio of the combustion system. From Equation 1 it can be seen that increasing the difference between T_2 and T_3 can increase the

efficiency of the cycle for the same pressure ratio. The thermal efficiency can also be written in terms of pressure ratio, r , as in Equation 2. The rotor inlet temperature cannot be increased indefinitely due to material limitations of the components used in the engine. The inlet temperature has been above the material allowable limits for many years and is an achievement accomplished solely due to the vast research into advanced cooling and materials for gas turbine components. This cooling is not without penalty however, as the high pressure air required to survive the tortuous cooling passages comes from the compressor itself and represents a direct parasitic impact on the total output of the engine. However, the gains in efficiency resulting from the use of firing temperatures higher than material limits offsets the output penalty in using bleed air from the compression stage, making it a ‘necessary evil’.

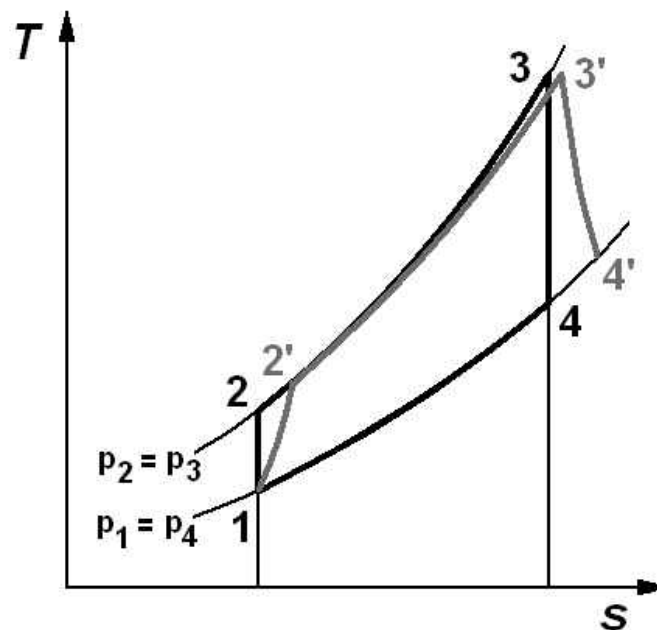


Figure 1: Brayton Cycle and the deviation from ideal performance

Equation 1: Thermal efficiency of the Brayton cycle

$$\eta_{th} = 1 - \frac{c_p(T_4 - T_1)}{c_p(T_3 - T_2)} \quad (1)$$

Equation 2: Thermal efficiency in terms of pressure ratio, r

$$\eta_{th} = 1 - \frac{1}{r^{(k-1)/k}} \quad (2)$$

Without an exhaustive review of the individual contributors to efficiency, the inlet temperature and thermal efficiency have risen from about 700 C and 20 % in the 1940's to 1600 C and >40 % of present day. (Higman 2003, Lefebvre 1999) These would not be possible without the advances in nickel based alloys, thermal barrier coatings, internal impingement and convective cooling, film cooling, and advanced aerodynamics. The mitigation of pressure loss throughout the engine and the increase in temperature ratio are often treated as the two primary thrust of advancing gas turbine technology. Though these are often treated separately, some coupling is apparent in various locations in the engine.

Flow Management

In order to operate modern gas turbines the primary and secondary gas paths need to be managed with minimal pressure loss to maintain efficiency. The secondary flows are necessary not only for cooling but maintaining dynamic seals between the rotating and stationary components. This sealing acts to prevent hot gas ingestion into unprotected cavities, thus

preventing the catastrophic failure of the engine. The total pressure of the secondary and primary flows are such that the fluid can maintain its determined flow rate for either power, cooling, or sealing considerations. There are often at least two compressor bleed points in a typical 14 stage compressor representing two or more pressure requirements for the secondary flow as shown in Figure 2. Typically 60% of the total work of the turbine stage is used to operate the compressor. (Boyce 2006) As such, the removal of the flow which has been worked upon from the work producing combustion stage is a significant penalty to the total output of the engine. Therefore the secondary flow for the lower pressure regions of the engine are taken earlier in the compressor section, and flow requiring a higher pressure budget is taken from the latter stages representing a more 'expensive' location in terms of output penalty. The highest flow requirements are often the combustion basket, 1st stage vane, and first stage blade. These components are often fed from the MidFrame cavity which contains the highest pressure air (read; the most expensive) as it is downstream of the last stage of the compressor. The required total pressures are calculated via complicated 1-D flow networks which require extensive calibration to achieve to proper flow rates. This often results in highly proprietary codes used for each company based on years of prior experience and research into new sealing technologies. The management of flow is of great interest since the more accurate the flow rate and total pressure budget (less unnecessary overhead), the higher the power output of the engine. This presents a challenging balance between cost, component life, and performance.

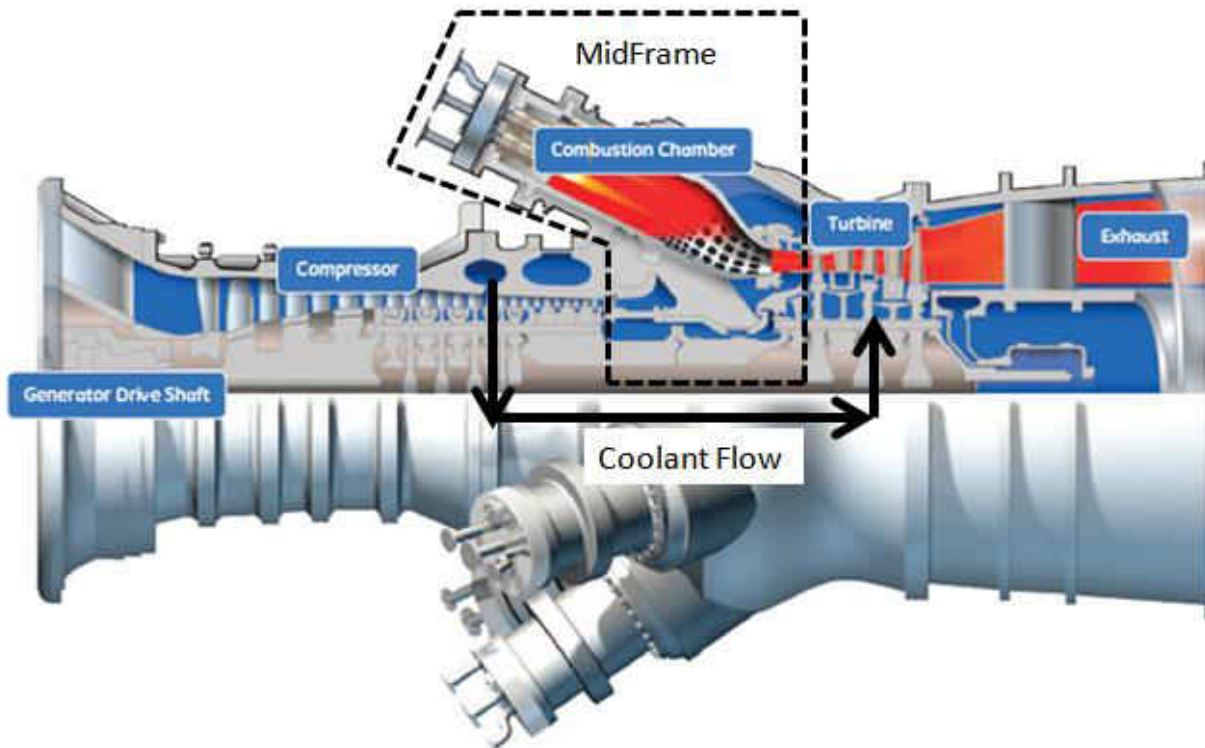


Figure 2: Example of the coolant flow and MidFrame location on a GE gas turbine

The MidFrame

The MidFrame (or combustor-diffuser system) represents the main gas path from the compressor exit through the combustion system to the turbine inlet. The role of the MidFrame is to direct the flow from the compressor into the combustion system with minimal pressure loss and high uniformity while supplying high pressure coolant flow to key high temperature components. This region looks quite different between aero propulsion and power generation due to the differences in geometric constraints and combustion orientations. These differences are illustrated in Figure 3. The volume and weight constraints of the aero propulsion counterpart

offer less opportunity for diffusion prior to the combustor inlet; a tradeoff designers have to accept. In the land based engine, the primary goal is efficiency and component life, though plant and material costs are reduced by reducing the footprint of the engine presenting a similar but less restrictive tradeoff as in the aero engine. The land based variant in particular represents one of the most complex flow domains of the entire engine. A schematic of the flow path is shown in Figure 4.

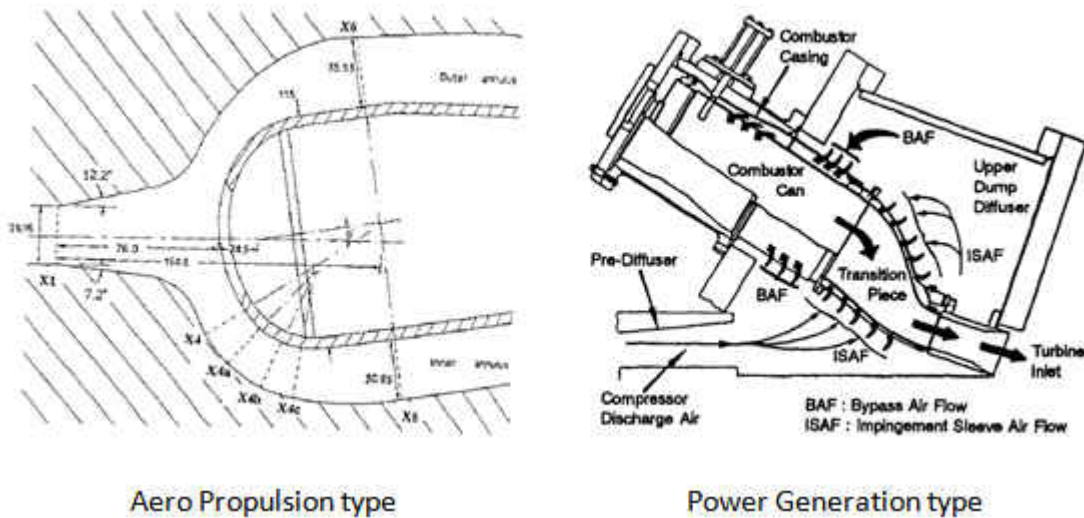


Figure 3: Difference between aero and power gen MidFrame geometries

The high pressure air enters the compressor exit diffuser (CED) after the last stage of compression with a high velocity, often skewed towards one endwall (outer diameter - tip or inner diameter - hub) or both. The flow contains wakes or momentum deficits from the outlet guide vanes of the compressor. The flow is highly turbulent as a result. The CED acts to reduce velocities and increase static pressure before entering the dump diffuser of the main MidFrame sector. The influence of CED performance on MidFrame sector flows and combustor inlet characteristics is not well understood in the literature. Designers of course prefer optimum

performance in the CED but at part load conditions velocity profiles can be different leading to less than optimal performance of the CED and in extreme cases potential flow separation. After the CED the flow encounters the CED support strut which provides support for the combustor shell casing. This bluff body interaction is one clear instance of flow unsteadiness as vortex shedding behind the strut feeds directly into the rest of the cavity. Different from the conventional cylinder in cross flow however, the strut geometry is complex and further, the velocity profile is tip strong which presents some difficulty when developing a non-dimensional vortex shedding frequency. Which value of velocity can be used? Which length scale is appropriate? This complexity reoccurs throughout the MidFrame when trying to cast it against simple flows and geometries as found in the open literature.

After the bluff body interaction of the CED strut, the flow impinges directly into the transition duct which carries the expanding combustion gases to the row 1 vanes. This presents one of the highest heat loads in the entire engine as the cooler compressor discharge impinges against the metal which encloses the hottest gas temperature in the engine. The values of heat transfer coefficient in this impingement region are difficult to model in computational fluid dynamics (CFD) codes due to the stagnation point anomaly whereby the turbulent kinetic increases to non-physical values. (Durbin 1996) Another difficulty regarding cooling of the transition (which relies on the pressure difference between the hot gas path and MidFrame dump cavity) as the flow impinges in one area, leading to high static pressures on the coolant side, and squeezes through the contraction provided by adjacent transition ducts leading to low static pressures (known as a Venturi effect). This non-uniform source pressure on the coolant side must be taken into account when designing effusion cooling of the transition duct as flow reversal is

possible for adverse pressure differences. Hot gas ingestion in gas turbine components can lead to catastrophic damage very quickly. The wake region of the transition is another suspected highly active unsteadiness region in the MidFrame.

After the transition impingement, the flow turns toward the combustor portal. The support strut for the transition (sometimes called the bull horn) represents yet another highly unsteady interaction as flow passes through the complex geometry. The flow then enters the annular passage of the combustor portal where it encounters a fuel mixing region. This stage of pre-mixing the fuel and air is referred to as the C-stage premixing region. It encompasses a ring near the center radius of the flow annulus. The purpose here is to promote turbulent mixing so the unsteadiness behind the C-stage ring is necessary. The flow then makes a 180 degree turn into the pre-swirlers of the combustion basket. The pilot and main fuel injectors and basket support struts all lead to more unsteady flow interactions. The combustion process then occurs and the hot gas products expand rapidly through the transition and into the row 1 vanes.

These diffusion, bluff body interaction, impingement, streamline curvature, Venturi effect, recirculation, and heat transfer effects all provide for a very complex and diverse flow domain which is not well understood.

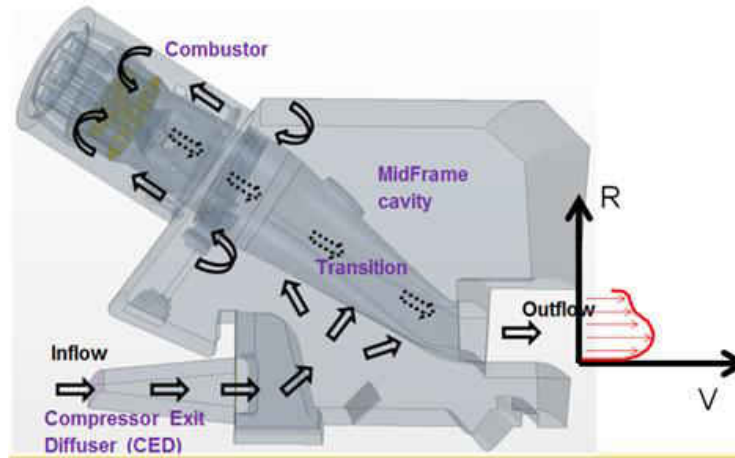


Figure 4: Flow pattern of land based MidFrame

EXISTING WORK

MidFrame and combustor-diffuser systems in land and marine based gas turbines are not as frequent in the open literature due to the uniqueness of each geometry. Whereas for heat transfer and cascade aerodynamics the geometries can be very similar among original equipment manufacturers (OEMs), MidFrame geometries vary greatly and are difficult to generalize in even a non-dimensional sense. Nevertheless, some of the pertinent works are summarized for both the aero-propulsion and power generation engines since the roles are the same, even if the geometries look dissimilar. Walker et al. studied an advanced hybrid diffuser (also referred to as vortex controlled diffuser) for use in aero type gas turbine combustor-diffuser systems. The authors reported an approximate 13% increase in overall C_p for the hybrid diffuser. Karki et al. used the standard k - ϵ turbulence model for a computational study of an aero type combustor-diffuser. The authors noted significant 3-D flows but also noted that axi-symmetric models predicted pressure recovery and total pressure loss reasonably well. Carotte et al. studied another aero type combustor-diffuser system with a short faired diffuser geometry which was successful in reducing the total pressure loss by 40% over the baseline design.

Orth et al. evaluate study a compressor exit diffuser (CED) for a medium power generation type gas turbine with a 10 stage axial compressor with a single stage centrifugal compressor at the end. They show the impact of CED performance as a component in the overall compressor performance through cycle calculations indicating that the overall compressor efficiency can be improved by 0.8% if the single stage centrifugal compressor can be increased 4% by way of CED optimization. Agrawal et al. investigate probably the most related

geometry to that which will be covered in the current study. The MidFrame is a 360 degree 1/3 scale model with one combustor instrumented. Also presented are some early computational fluid dynamics (CFD) results for comparison. The authors report velocity profiles at several locations throughout the MidFrame offering insight into the Venturi effect between transitions among other characteristics which will present themselves in the current work. The exact behavior of separated flow is very hard to predict as seemingly small influences can have dramatic results in the separation point and attachment location. Kibicho et al. studied the flow in a wide angled diffuser identifying the velocity profiles at several streamwise locations as well as the pressure recovery coefficient of the separated rectangular diffuser when the flow was forced to attach to either side. No unsteadiness measurements were obtained in this experiment. Mahalakshmi et al. report velocity profiles, turbulence intensities, and static pressure recovery for a conical diffuser with wakes at the inlet. The authors report a marginal increase in pressure recovery for small angle diffusers but no impact for larger diffuser angles. Cherry et al. reported the geometric sensitivity and progression of flow separation two rectangular diffusers using a water tunnel and magnetic resonance velocimetry (MRV).

The crux of the unsteadiness measurements in the current work rely on velocity and pressure fluctuation comparisons. There has been some similar work done primarily Ying Zheng Liu group at Shanghai Jiao Tong University. Liu et al. study turbulent wall bounded shear using joint pressure-velocity measurements and were able to identify the shedding frequency successfully. Ke et al. used an array of static pressure microphones on the landing region behind a backward facing step with and without flow entrainment. The authors were able to identify the shedding frequency Strouhal number at 0.076. Liu et al. investigated separated and reattaching

flow over a two-dimensional square rib. The authors identified high fluctuations in wall static pressure and the large scale vortex shedding Strouhal number of 0.03. Zhang et al. studied the wall pressure fluctuations of separated and reattaching flow behind the leading edge of a blunt edged flat plate. The authors successfully identified two dominant Strouhal numbers for the large scale shedding frequency of vortices and the unsteady wake region at 0.118 and 0.162 respectively.

MOTIVATION

The MidFrame region of the gas turbine plays an important role in overall engine efficiency and cooling aspects. In design, it usually results in a tradeoff between structural integrity, manufacturability, ease maintenance/assembly, cost, and performance. It represents one of the most complex flow domains in the entire engine. This complexity leads to a void in such experiments in open literature due to the uniqueness of the type of rig and the applied nature of the problem. Nevertheless, such a complex applied experiment is very beneficial to the intellectual and scientific community in relating the simple geometries tested by Zhang et al. for instance. The flow characteristics of the MidFrame affect the compressor diffuser performance and combustor inlet flow quality in particular. The inlet cases chosen represent a sort of sensitivity study to evaluate the resilience of a typical power generation type MidFrame. Flow unsteadiness in the combustor inlet can cause serious damage if the fluctuations allow the flame front to propagate outside of the thermally protected combustor basket. These types of time accurate measurements are not often possible in actual engines or unsteady simulations due to time or instrumentation limitations. This resilience of the MidFrame to inlet conditions in both the mean and time accurate sense and quantification of unsteadiness are the primary results of the current work.

EXPERIMENTAL PROCEDURE

Steady Instrumentation

The rig itself is a full scale model of a 1/16th sector of an actual gas turbine, specifically the Siemens SGT6-5000F(D2). Its construction is machined aluminum for the primary support structure with reinforced acrylic walls for optical access. The geometry matches nearly exactly with the actual engine. The rig contains actual engine hardware for the combustor basket and transition piece. The CED support strut is located at the centerline of the domain, with equal flow area on either side. The rig is operated under suction using a 75 kW (100 hp) blower capable of 40 inches water in pressure head. The incoming flow is conditioned using a two stage annular nozzle with screens and honeycombs according to Mehta and Bradshaw. (Mehta and Bradshaw 1979) The flow then is modified using the inlet velocity profile screens if applicable for the appropriate case. The locations of the two different screen types are indicated in Figure 6. Also shown is the location of the inlet traverse which will be described shortly. After the rig, an exhaust diffuser is used to recover dynamic head before turning towards the blower. The exhaust diffuser exits into a large rectangular plenum before re-entering a circular duct which leads to the blower inlet. A rubber flange section of the circular duct is used to decouple the duct from blower vibrations. The large plenum chamber also is used to dampen rig frequencies and prevent communication of these frequencies upstream into the measurement domain. The flow path through the diffuser and plenum is shown in Figure 5.

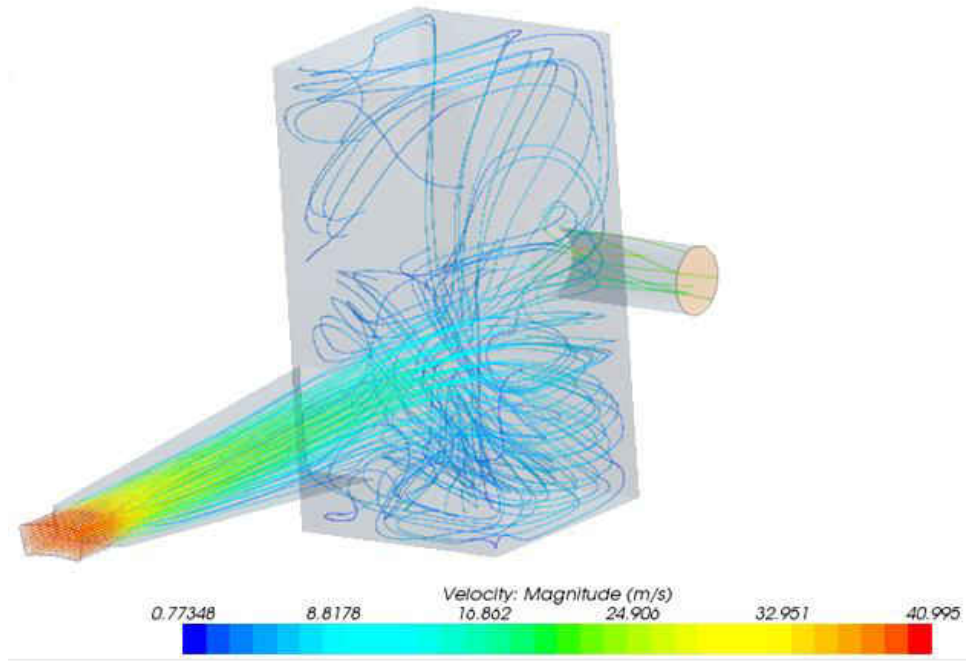


Figure 5: Streamlines through the exhaust diffuser and plenum chamber

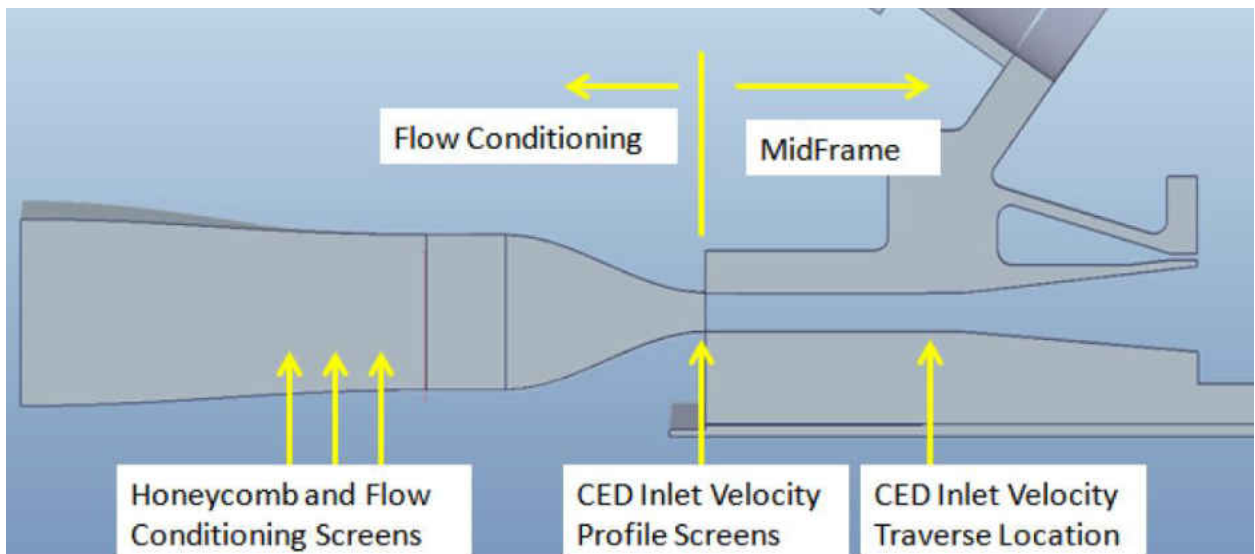


Figure 6: Location of flow conditioning screens relative to the velocity profile screens

The general flowpath through the MidFrame domain is illustrated in Figure 8. In order to characterize the inlet conditions in detail, the velocity profile is mapped using two separate Pitot-static probes. The first is a 1.59 mm diameter probe which is simply supported on two vertical traverses on either side of the inlet to the rig. This small diameter probe is used for the rectangular portion covering most of the annular inlet. Because of the small diameter the probe must be supported from both sides. A rendering of the small diameter probe traverse is provided in Figure 7. Differential pressure is measured using a conventional diaphragm transducer with a full scale range of ± 6.8 kPa. The inaccessible corners of the annular section are measured using a larger 6.4 mm probe which is traversed in a cantilever fashion from the nearest sidewall to prevent unnecessary blockage of the inlet channel resulting in flow acceleration. Pressures are measured using the same transducer as the small diameter probe. The two individual traverses are combined to represent the most complete representation of the inlet velocity contour possible.

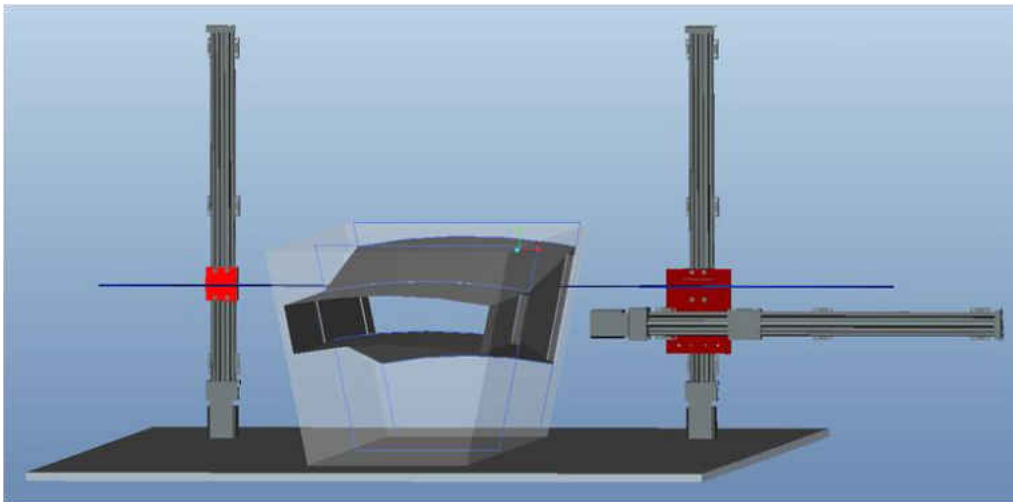


Figure 7: Rendering of the dual support small diameter Pitot-static probe traverse

In order to establish the level of CED separation in a qualitative sense, microtufts are applied to the bottom, sides, and top of the CED. These 0.025 mm monofilament nylon threads are glued at one end to the given surface. The small diameter and relatively low stiffness allow the thread to follow the local flow direction. These provide good indicators of the occurrence of separation.

In order to test the impact of inlet conditions on the MidFrame, the inlet condition must first be modified. Through the use of the inlet conditioning system, a low turbulence uniform velocity profile is achieved. This uniform velocity profile leads to severe flow separation on the bottom wall of the CED. This case is referred to as the Separated Bottom (SB) case. In order to force a fully attached flow in the CED, the momentum is redistributed towards the outer and inner diameter for the constant area average Mach number. The resulting velocity profile is commonly referred to an endwall strong velocity profile and can reflect a more realistic engine representative velocity profile in some cases. This case is referred to in the current work as the Fully Attached (FA) case. A summary of the inlet conditions is provided in Table 1. This velocity profile is achieved by added resistance to the mid-channel radius via screens. The screens used are summarized in Table 2. The coarse screen is steel wire mesh used mainly for support of the fine nylon screen which provides most of the resistance. The mesh size characteristic is a screen manufacturing standard which defines how many mesh squares fit in a linear inch in both directions. For example, the coarse screen will have 4 mesh openings per square inch.

Table 1: Summary of inlet conditions



Nomenclature	Notes	Image
Fully Attached (FA)	Higher resistance at midspan causes higher momentum at tip/hub resulting in attached flow	
Separated Bottom (SB)	Low turbulence intensity and uniform velocity profile lead to separation on bottom CED wall	

Table 2: Summary of screen characteristics

Screen	Mesh Size	Open Area Ratio (β)	Pressure Drop Coefficient (K)	Wire Diameter (mm)
Fine	7.9x7.9	76.40%	1.488	0.851
Coarse	2x2	55.00%	0.404	1.6

Static pressures are measured on the CED bottom and sidewall via 0.8 mm diameter drilled pressure taps. Pressure measurements are taken with a Scanivalve multiplexor with a single 20 inch water transducer. These static pressures are normalized as static pressure coefficients as in Equation 3 where the inlet dynamic head is calculated using the average inlet velocity and density and the P1 values is taken from the average of five static pressure taps at the inlet of the CED. The schematic showing the CED bottom static pressure taps is located in Figure 9.

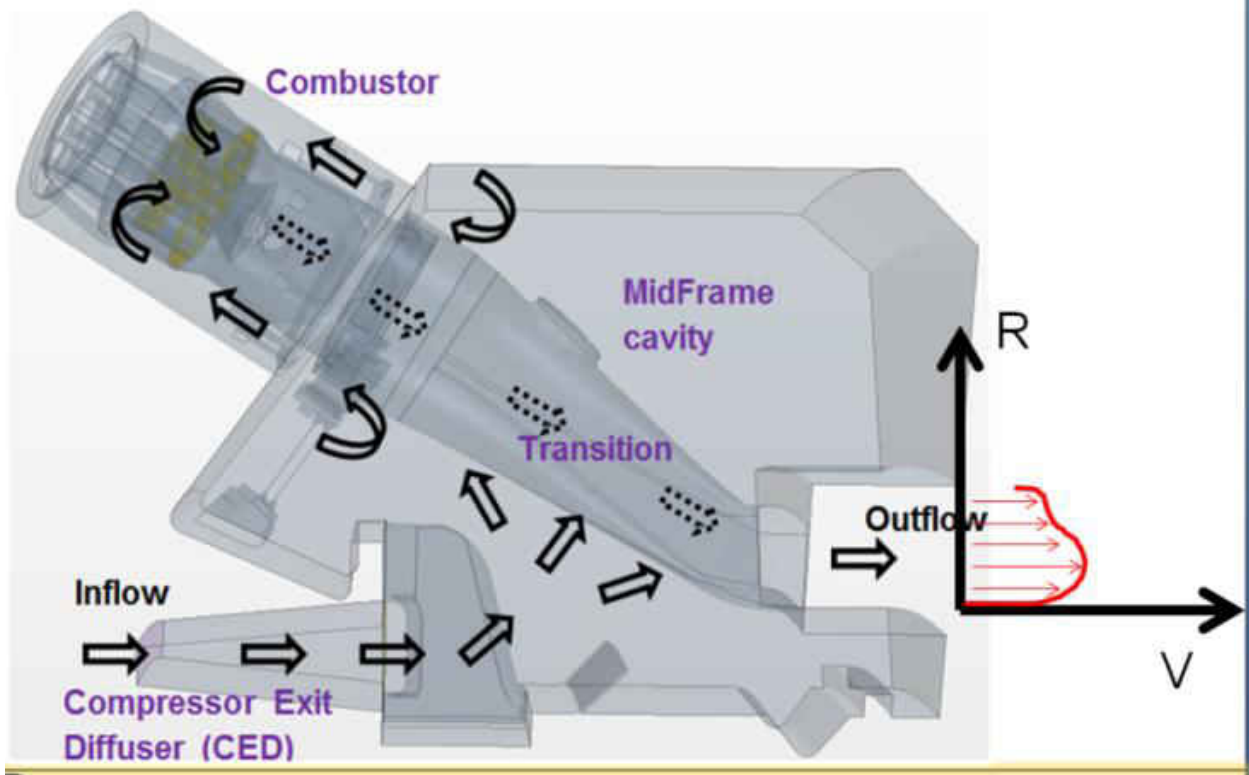


Figure 8: Flow schematic of the main MidFrame

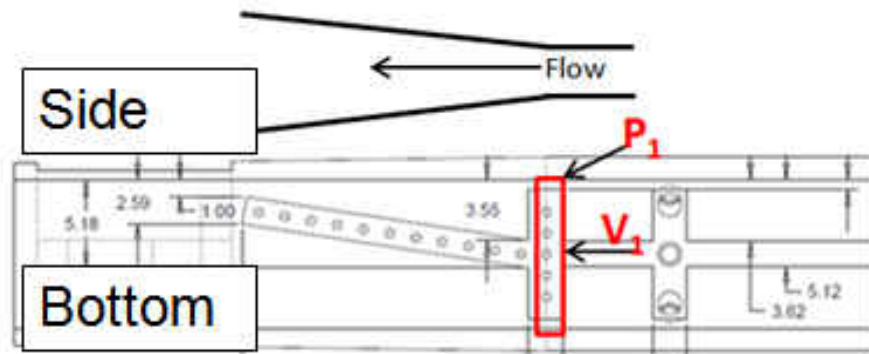


Figure 9: CED bottom wall static pressure taps

To visualize mean flow exiting the CED, an array of sidewall static taps are positioned to calculate pressures in this region. The schematic locating to the pressure taps along the CED

sidewall and CED exit regions is shown in Figure 10. The transducer and multiplexor are the same for the CED walls. Static pressure taps are also placed in the combustor portal region in several groups. The first set of groups is located at 4 circumferential locations, consisting of 10 at each location in the axial direction. These are located at $\pm 22.5^\circ$ as indicated in Figure 11, and also at $\pm 157.5^\circ$ which is not shown in the figure.

In order to quantify the flow uniformity in the combustor portal, custom designed total pressure probes are used which have Kiel type heads to reduce the sensitivity to inlet flow angle. These designs were developed by Siemens Energy, Inc. for use in actual engine tests and were provided for use in the rig. Previous calibrations against reference Pitot-static probes show no deviation in sensed total pressure between $\pm 45^\circ$. The long length of the probes allows measurements at 8 circumferential locations in the combustor portal. The probes can be traversed in the axial direction as well, allowing for a wide range of possible measurement locations in the combustor portal. A cross section of the Kiel probe is shown in Figure 12 along with an image of the instrumented combustor portal.

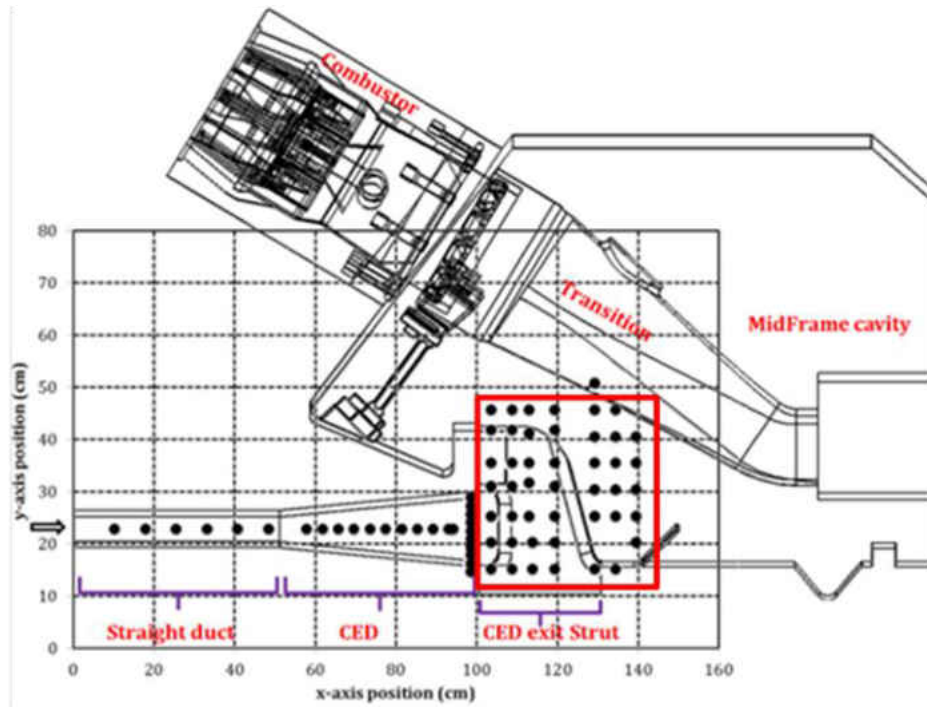


Figure 10: CED sidewall and CED exit region static pressure tap locations

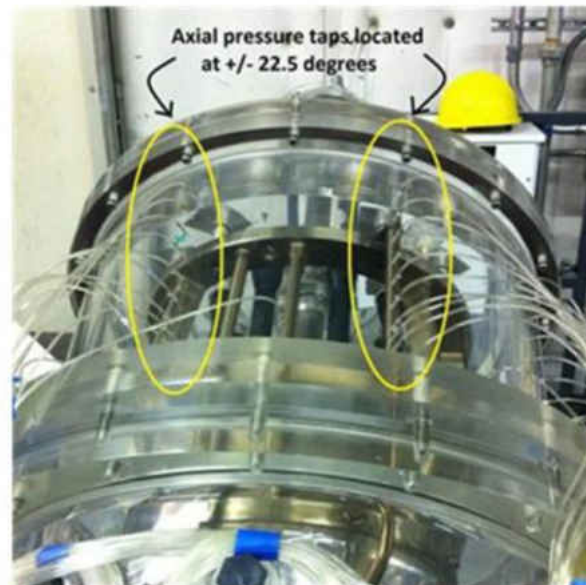


Figure 11: Location of two of four rows of static pressure taps in the combustor portal

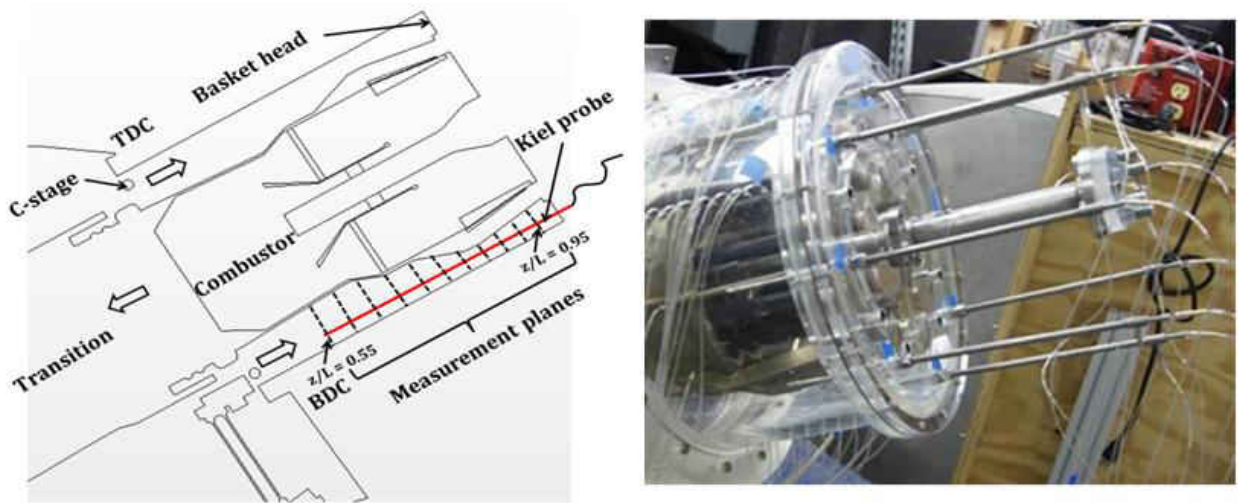


Figure 12: Cross section of Kiel probe measurement planes (left) and image of instrumented combustor portal (right)

With a rig such as the current one, with the degree of complexity and relatively high mass flow of ~ 2.7 kg/s, an accurate measure of mass flow and confirmation of the constant area average Mach number presents some difficulty. The inlet traverse resolution was not fine enough to simply area average the values for each inlet condition. In particular, the high gradients of the FA case would contain some uncertainty when used in the calculation of area average velocity and eventually mass flow rate. It was determined that if a location in the rig could be shown to contain a self similar velocity profile, that is, a velocity profile which did not vary for vastly different inlet conditions, this location could be used to correlate with the area average velocity at the CED inlet. Such a location was shown for the transition exit (the outflow location in Figure 8). Here the velocity profile was very similar for the two inlet conditions. At this stage, a single radius can be used to measure velocity. This single point velocity measurement can be related to the area average inlet velocity which is obtained via the traverse at the CED inlet for the SB case (uniform velocity profile). After the single point velocity value is correlated to the area average

velocity at the CED inlet, this correlations can be used for any highly skewed inlet velocity condition. The correlation is shown in Figure 13. The transition exit profile is shown for the two inlet conditions tested in Figure 14.

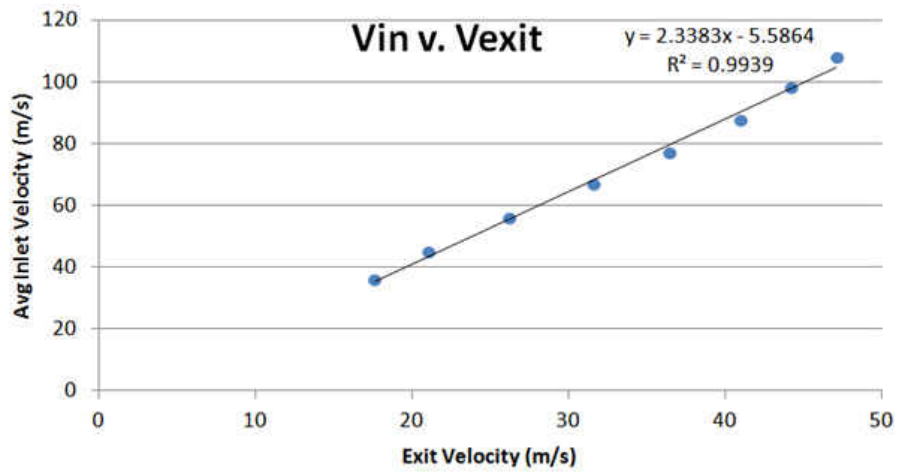


Figure 13: Inlet area average and transition exit single point velocity correlation

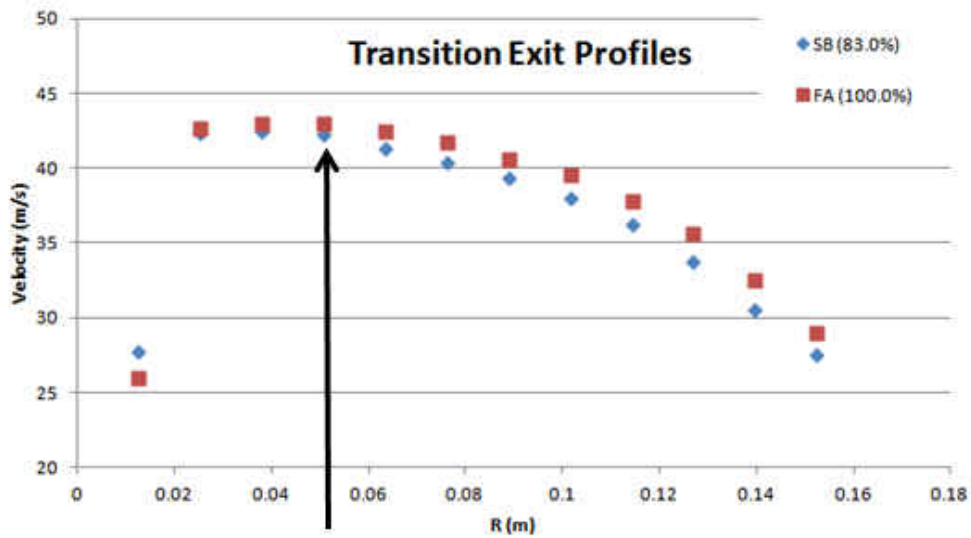


Figure 14: Transition exit velocity profiles and single point measurement for correlation denoted

Unsteady Instrumentation

In order to quantify the unsteadiness in the MidFrame, several techniques are used. The first of which is the constant temperature anemometer (CTA) or hotwire. This technique uses a TSI brand 50 μm diameter tungsten wire which is connected to a Wheatstone bridge. The wire is heated to a temperature above ambient and maintains a particular electrical resistance. The cooling effect of the ambient flow acts to reduce the temperature and thus the resistance of the wire. The Wheatstone bridge voltage changes as a result, at which point the anemometer adjusts the voltage to bring the wire back to the constant temperature target. This process can be repeated up to 300,000 times a second which provides very fast response to changes in ambient velocity. The hotwire is calibrated using a uniform jet. In this manner, the calibration curve between velocity and voltage output is achieved. The time series of velocity can be transformed using the Fast Fourier Transform (FFT) to the frequency domain where the dominant periodic fluctuations are easier to identify. The hotwire is useful for measuring local unsteadiness locations but is only used in locations where accessible.

The other unsteady instrumentation used is the Bruel and Kjaer brand high sensitivity static pressure microphone. These microphones have a thin diaphragm which changes resistance depending on the degree of deflection. The frequency response can provide pressure measurements at rates up to 400 kHz. The pressure signal measured is the differential pressure fluctuation about a reference pressure which in the case of the current work is ambient outside of the rig walls. Five of these microphones are measured simultaneously using a 16 bit analog to digital converter (ADC) and data acquisition system (DAQ) by National Instruments. This

provides high resolution measurements of the pressure fluctuations within the rig. The same FFT application is used with the microphones to achieve the frequency spectrum and amplitudes of the pressure fluctuations.

Additionally, wall mounted accelerometers are used to determine rig vibrations as opposed to flow unsteadiness. Early tests indicated that the wall mounted microphones were also acting as accelerometers to the wall. A measurement was necessary to separate purely wall vibrations from those that are purely flow based unsteadiness. The three axis accelerometers signal is measured simultaneously with the microphones. The two signals are included in a cross spectral density function to calculate the Coherence of the two signals. The coherence function is shown in Equation 3, and relates the degree of similarity between the two signals in the frequency domain. A coherence of 1.0 means exact match of the particular frequency while 0.0 means the two signals do not match at the given frequency. Using this function, frequencies which are common to both the accelerometer and microphone signals can be taken as wall vibrations.

$$C_{xy} = \frac{|G_{xy}|^2}{G_{xx} G_{yy}} \quad (3)$$

This approach of neglecting frequencies which appear in both the wall mounted accelerometers and the static pressure microphones is not always appropriate however. There exists a complicated fluid-solid interaction known as acoustic lock-on where a flow unsteadiness frequency is influenced by an external forcing function. The wall vibration can act to force the frequency of the flow unsteadiness outside of what would otherwise be determined by the

velocity scale alone. Furthermore, the flow unsteadiness can cause wall vibrations as well. This presents some difficulty when analyzing complex spectra and attempting to decouple the wall vibrations from flow unsteadiness. For the time being, the frequencies which appear to be influenced by the fluid-solid interactions are not evaluated further. These interactions should be investigated in future works.

Apparent flow frequencies are identified from the FFT of the microphone signal, neglecting at first those that appear in the accelerometer as well. These frequencies are then compared to a range of potential sources using the open literature to determine the expected Strouhal number. The Strouhal number is a non-dimensional frequency which depends on geometry and Reynolds number and is shown in Equation 4. For the case of a cylinder in uniform velocity crossflow, the Strouhal number is commonly taken as 0.21 but in fact varies up to $\pm 10\%$ in the range of Reynolds numbers from 100 to 100000 where it is applied. Non-uniform velocity profiles further complicate the prediction of vortex shedding frequency by requiring the use of local velocity scale. These factors often lead to some scatter about the measured frequency.

$$St_D = \frac{fD}{V} \quad (4)$$

In order to validate the proposed measurement techniques the case of the simple cylinder in cross flow is used. The instrumentation is applied to a square cross section wind tunnel independent of the MidFrame rig. A Reynolds number of 26,200 is applied to the cylinder by

adjusting the fan speed. The hotwire is located about 5 cylinder diameters downstream at the centerline of the cylinder. A pair of microphone-accelerometers was mounted to the side walls at the same downstream location, one on the wall normal to the axis of the cylinder and the other on the wall parallel with the axis of the cylinder. These placements were chosen to evaluate the sensitivity of orientation of instrumentation to the strength of the signal. Figure 15 shows the schematic of the experiment. For the cylinder, the instrumentation on the wall parallel with the cylinder axis showed the strongest signals, though the other wall showed the same values with less amplitude. The result of this validation experiment is shown in Figure 16.

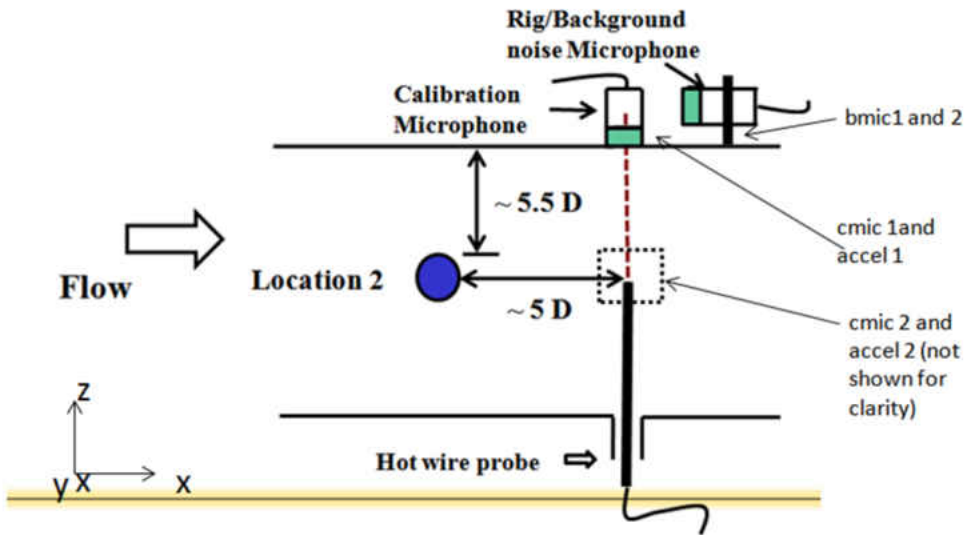


Figure 15: Schematic of unsteady instrumentation validation experiment

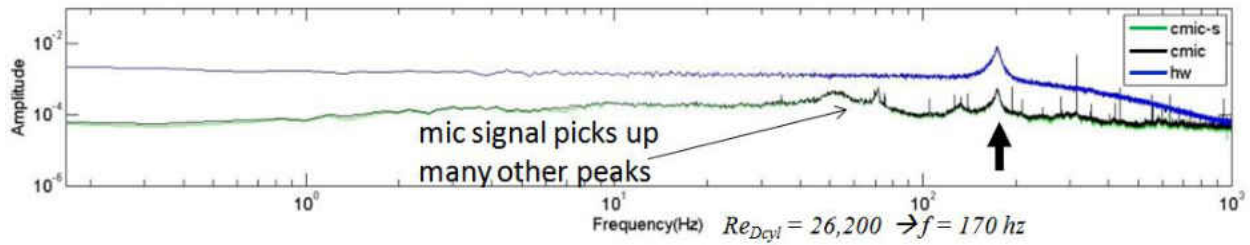


Figure 16: Results of unsteady instrumentation validation experiment

The results of the validation experiment show that the microphone and hotwire produce the same frequency as predicted by open literature to within ± 10 Hz. The microphone also shows many other frequencies that do not appear in the hotwire signal. These are a result of fan noise, wall vibrations, and possible background noise. This shows that the microphone can produce the same result as a well placed hotwire, if the correct frequencies can be identified among the other extraneous peaks. The microphone signal has a high degree of noise and small scale fluctuations which tend to obscure some peaks. In order to reduce the contribution of small scale peaks and obtain clean signals, a spectral averaging technique is applied. This method of reducing noise consists of breaking the time series into N_b bins of data each containing N samples with some overlap among the bins. An FFT is applied to each bin. The individual FFT's are then averaged and used in the spectral density yielding a much cleaner signal. There exists a trade off due to the fact that the signal is not continuous and the sampling time is not infinite. The lower frequency absolute amplitudes can be reduced due to spectral leakage where the bin size is not capturing as many of the lower frequency events as the original time series. For the process of identifying peaks and not necessarily comparing magnitudes, the spectral leakage does not change the peaks in the region of interest. Figure 17 shows the impact of spectral averaging on some sample spectra. The 80 bin spectral average can be seen to clean the signal much more so than the 4 bin

case but at the expense of reduced magnitudes in the lower frequencies. This processing technique will apply to both the velocity and pressure fluctuation spectra to facilitate identification of significant peaks. In addition to spectral averaging, multiple samples are taken for each microphone signal. Each of the individual spectral averaged signals are then arithmetically averaged together to produce a cleaner signal and reduce contributions from random fluctuations in the signal. An example of the overlaid signals and the resulting average signal is shown in Figure 18 using sample data from the CED microphone. All spectra including hotwire and microphone presented in the results will be treated using the above technique.

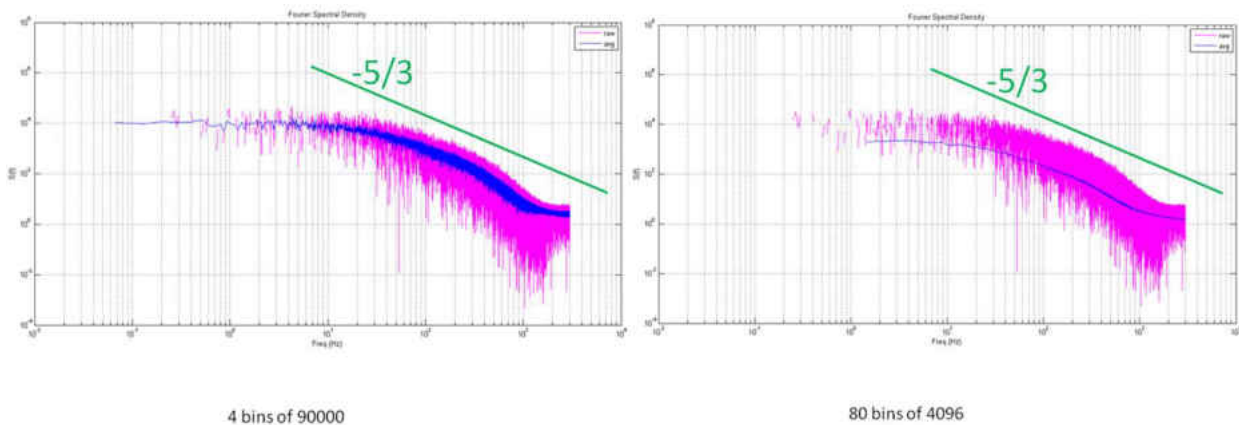


Figure 17: Influence of bin size on spectral averaging

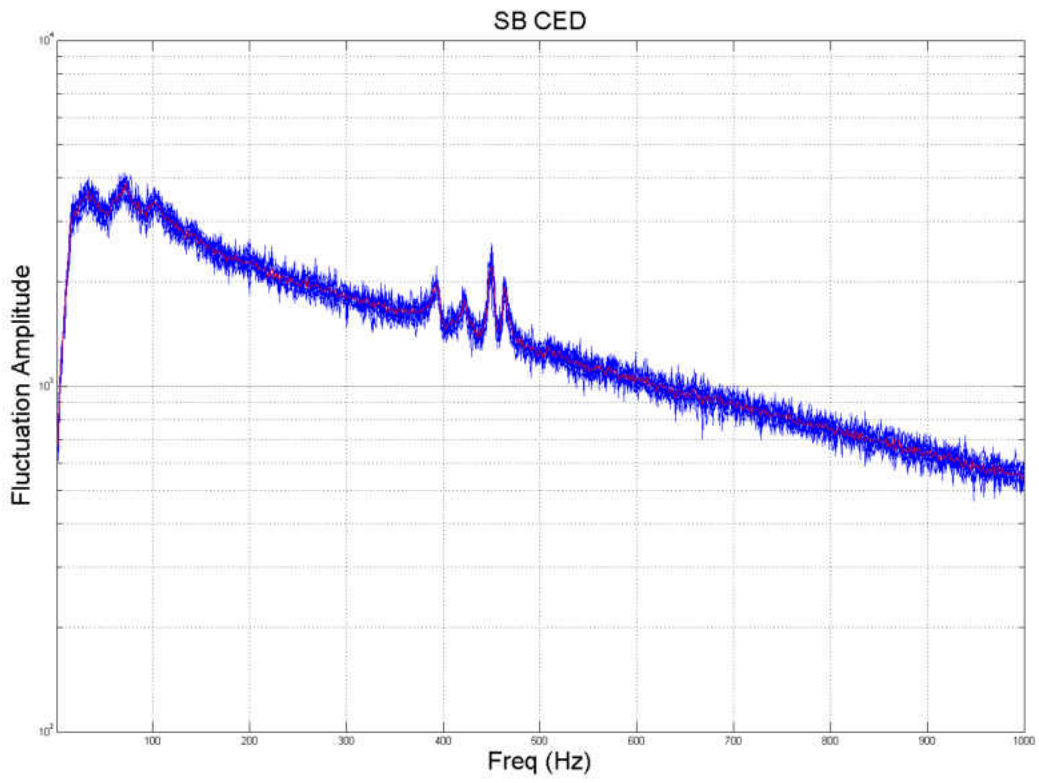


Figure 18: Ten raw overlaid signals (blue) with resulting clean signal using spectral and arithmetic averaging (red)

NUMERICAL SETUP

Numerical simulations were conducted using the commercial CFD mesher/solver code StarCCM+ version 7.06.009. The geometry matches very closely with the experimental rig. The domain is meshed using the unstructured polyhedral mesh with prism layers throughout. The guidelines provided by CD-Adapco regarding mesh quality including cell skewness angle and volume ratio were used to eliminate numerical diffusion or other influences of mesh on the solution quality. The mesh cross section through the centerline of the domain is shown in Figure 19 for reference. The domain used for the results presented included approximately 10E6 cells in total. A Reynolds Averaged Navier-Stokes approach using the Realizable $k-\varepsilon$ (RKE) turbulence model is used. The RKE model is known to under predict diffusion in the flow field but is one of the few that are robust enough to model the vast array of flow scenarios encountered including flow separation and impingement. The results are considered converged when the residuals achieve a level at least two orders of magnitude smaller than the initial values and the total pressure loss and CED C_p are no longer changing significantly with subsequent iterations.

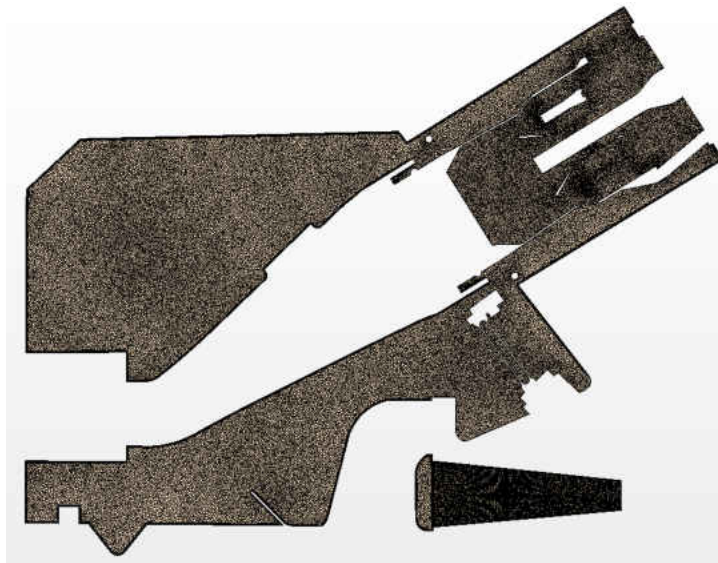


Figure 19: Centerline cross section of mesh

The boundary conditions are prescribed modeling the experimental work by mapping the velocity magnitude and turbulence intensity at the inlet section. The FA inlet condition is a simplified version of the experimental case which varies only in the radius, eliminating possible influence of measurement resolution and interpolation from the mechanical traverse. The inlet velocity profiles are shown in Figure 20. Turbulent viscosity ratio is left at the default value of 10 at the inlet. Total pressure and temperature are 101325 Pa and 300 K respectively. Figure 21 shows the overview of the domain with inlet and outlet denoted. Interfaces between discrete regions are shown in yellow. The flow through the transition was not modeled to reduce the mesh and computational effort as this part of the domain is anticipated to have little impact on the upstream regions.

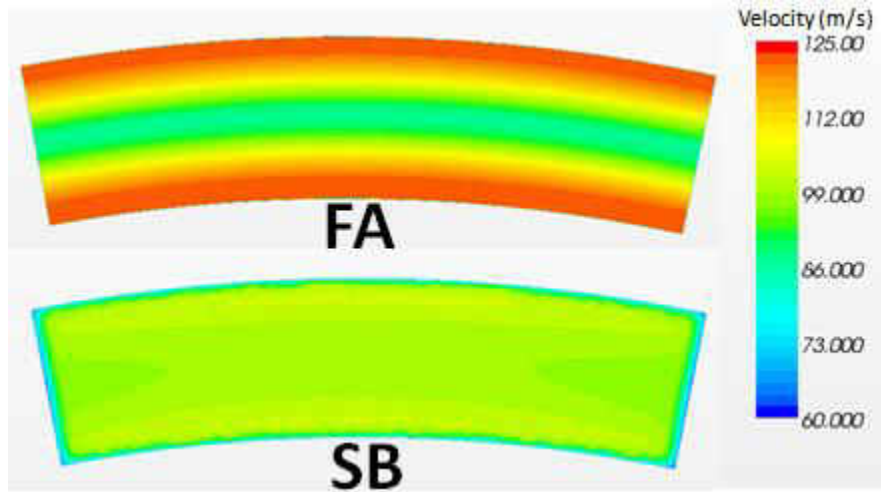


Figure 20: Simplified inlet profiles mapped from experimental cases

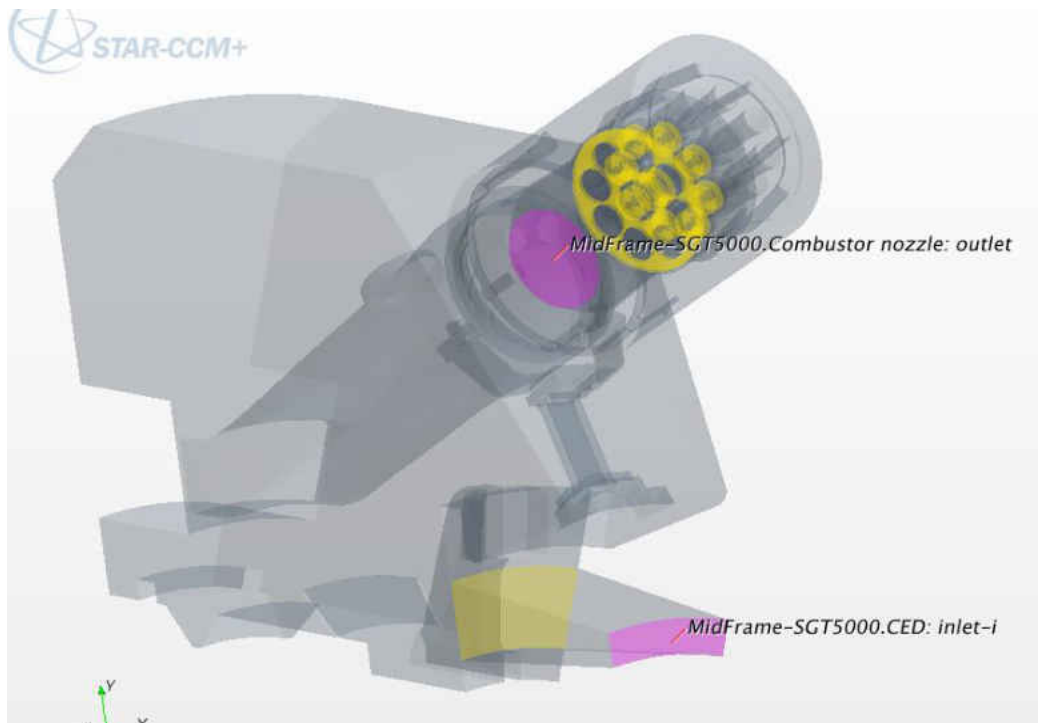


Figure 21: Overview of boundary conditions

RESULTS

Experimental Results

The role of the screen configurations is to impose a skewed velocity profile into the CED inlet. Figure 22 shows the images of the screen configuration at the inlet adjacent to the corresponding inlet velocity contour. The rectangular shape of the contour is clearly seen to miss some portions of the annular cross section. These data points must be filled in with an alternative probe traverse. These points are not included in the contours but are included in the raw CFD validation dataset provided. The FA case can be seen to be mostly a function of radius except very near the sidewalls. The SB case shows the uniformity of the inlet condition which leads to separation of the bottom wall. The result of these inlet velocity profiles is obtained via microtuft visualization on the bottom wall of the CED shown in Figure 23. The tufts in the FA attached case are easy to identify as they lay quite still on the bottom wall signifying attached flow. For the SB case they are harder to see as they oscillate rapidly in the separated flow field. The flow is seen to have consistently reversed near the bottom wall for the separated region.

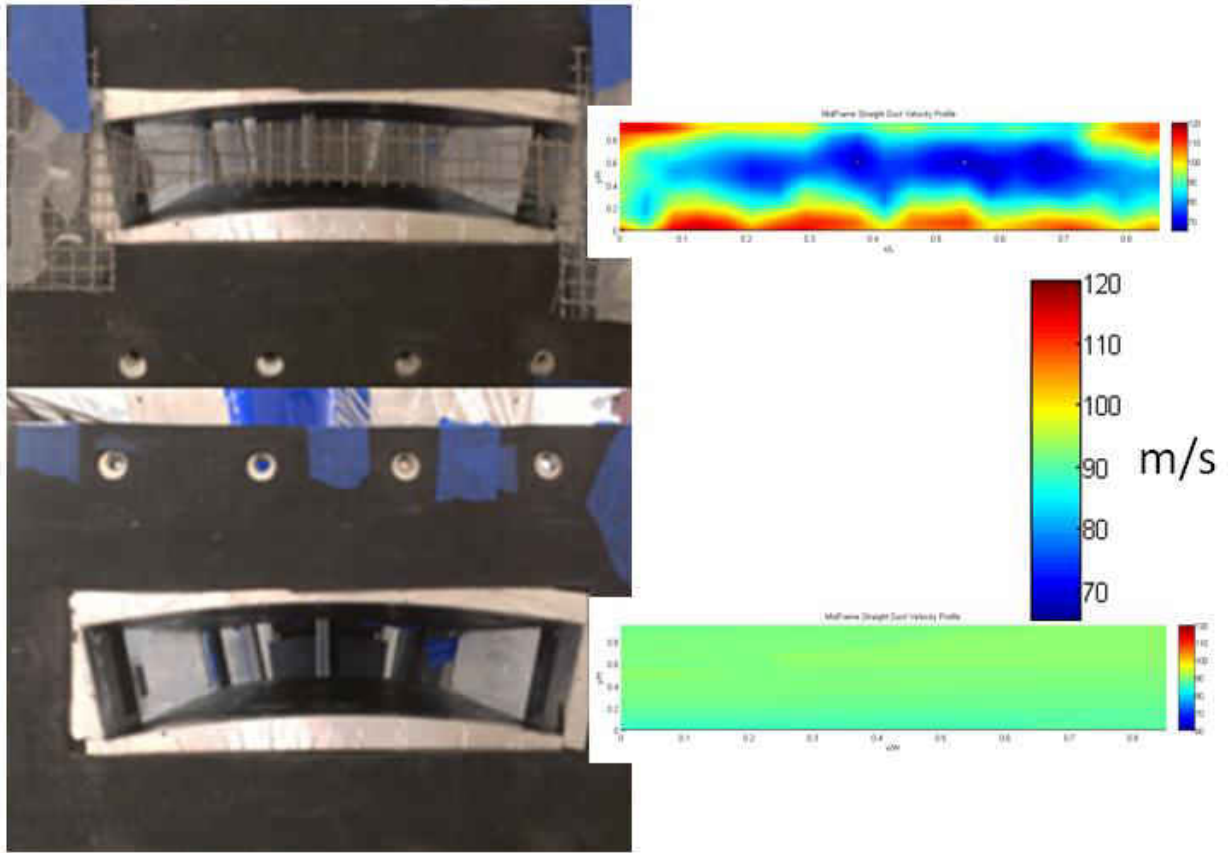


Figure 22: FA (top) and SB (bottom) inlet configurations and inlet velocity contours

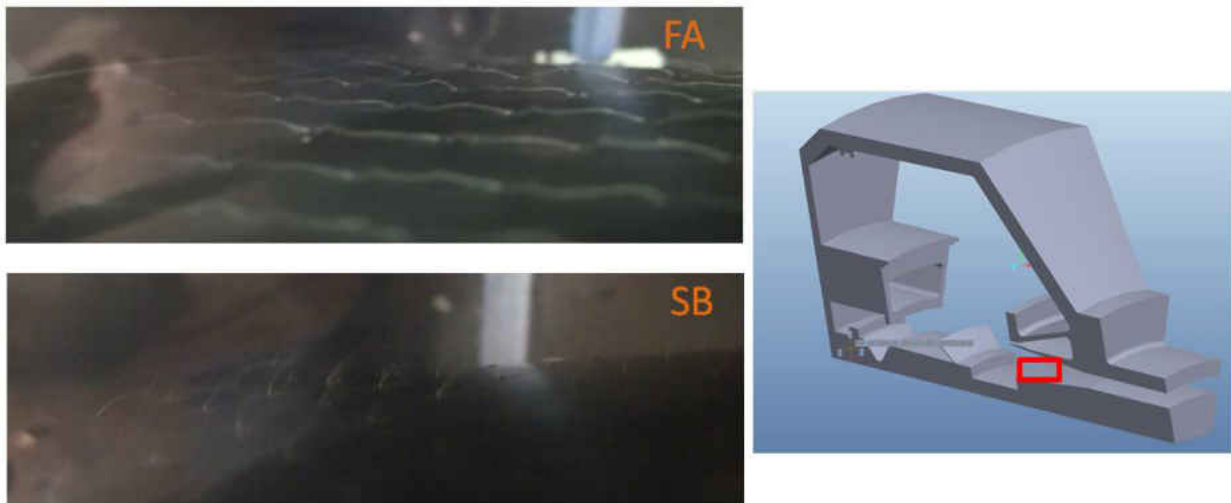


Figure 23: Microtuft visualization on bottom wall for the FA (top) and SB (bottom) cases

The radial turbulence intensity is measured at the CED inlet centerline. Figure 24 shows the comparison between both inlet conditions. The SB case has low turbulence intensity as a result of the upstream flow conditioning system while the FA case shows values of up to 3% where the screen wake region and velocity shear layers generate turbulent kinetic energy. The two inlet conditions correspond well in the region where the screen is not present (near the bottom wall). It is suspected that the turbulence intensity of the screens is a secondary contributor to the fact that the CED is attached for the FA case since the majority of the turbulence is constrained to the inner core of the duct at the CED inlet.

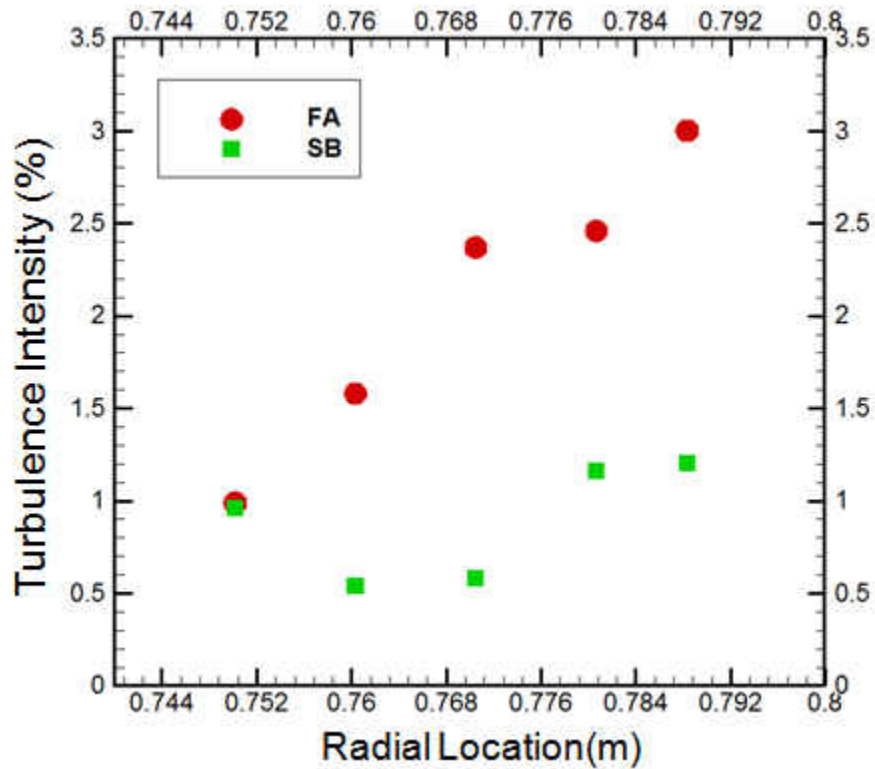


Figure 24: Turbulence intensity of CED inlet in radial direction for $\theta = 0^\circ$

The performance of the CED can be seen by measuring the pressure coefficient, C_p , using the bottom wall static pressure taps. Figure 25 shows the ideal C_p (using the area ratio) along with the C_p curves of the SS, SB, and FA cases. As expected the FA case has the highest pressure coefficients as it uses more of the geometric area ratio than the slightly lower performing SS case. The separated bottom has the worst performance as expected. The C_p at the exit of the CED determines the minimum of the dump diffuser (the main MidFrame cavity). When evaluating the sidewall C_p values just beyond the exit this offset in scales can be seen due to the drastic performance difference in the CED which feeds the rest of the cavity. The sidewall C_p contours are shown in Figure 26. The trends between the two inlet conditions are very similar. The main jet turning out of the CED can be observed in both cases. The relative minimum C_p of the turning jet is lower for the SB case where the jet contains higher maximum velocities due to the reduced effect area in which the jet occupies for the constant mass flow rate condition.

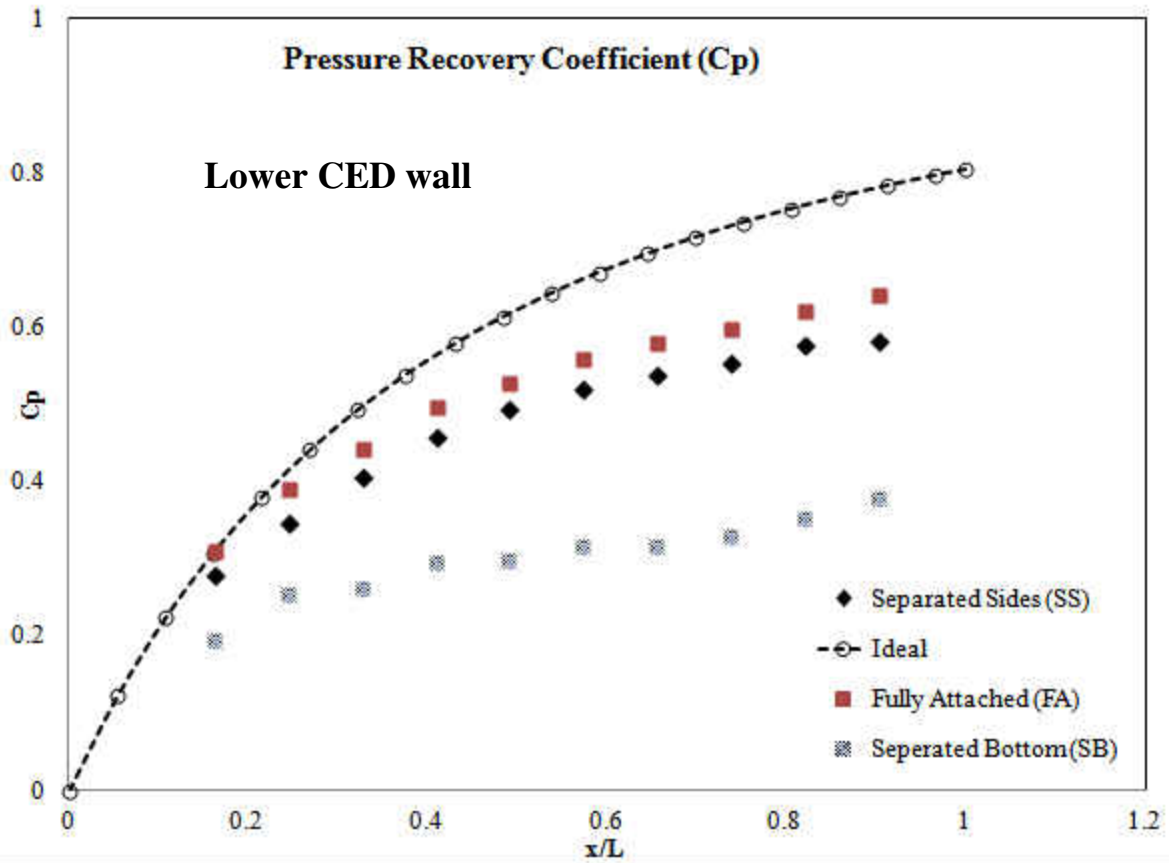


Figure 25: CED C_p curves using bottom wall static pressure measurements

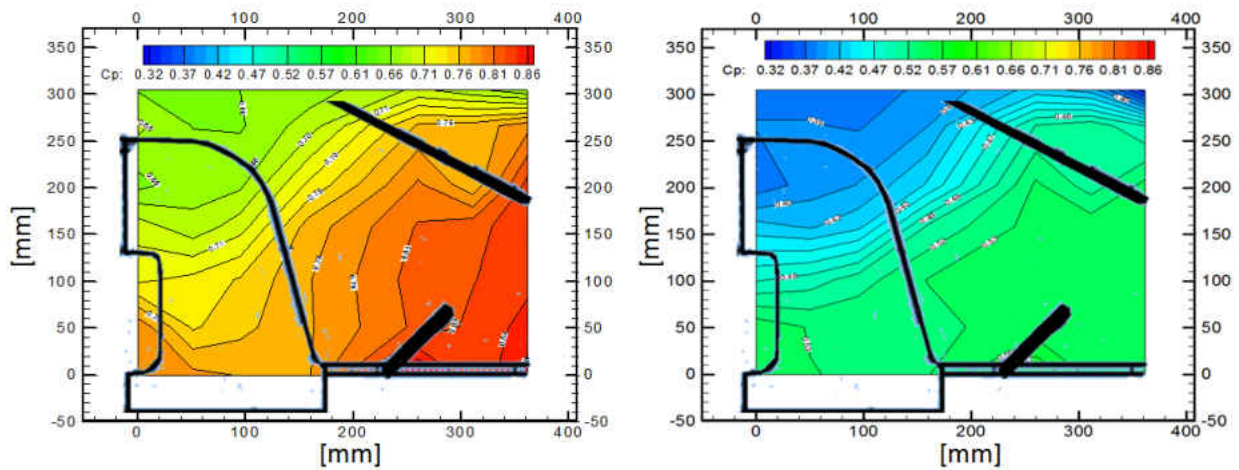


Figure 26: Sidewall C_p measurements at exit of CED

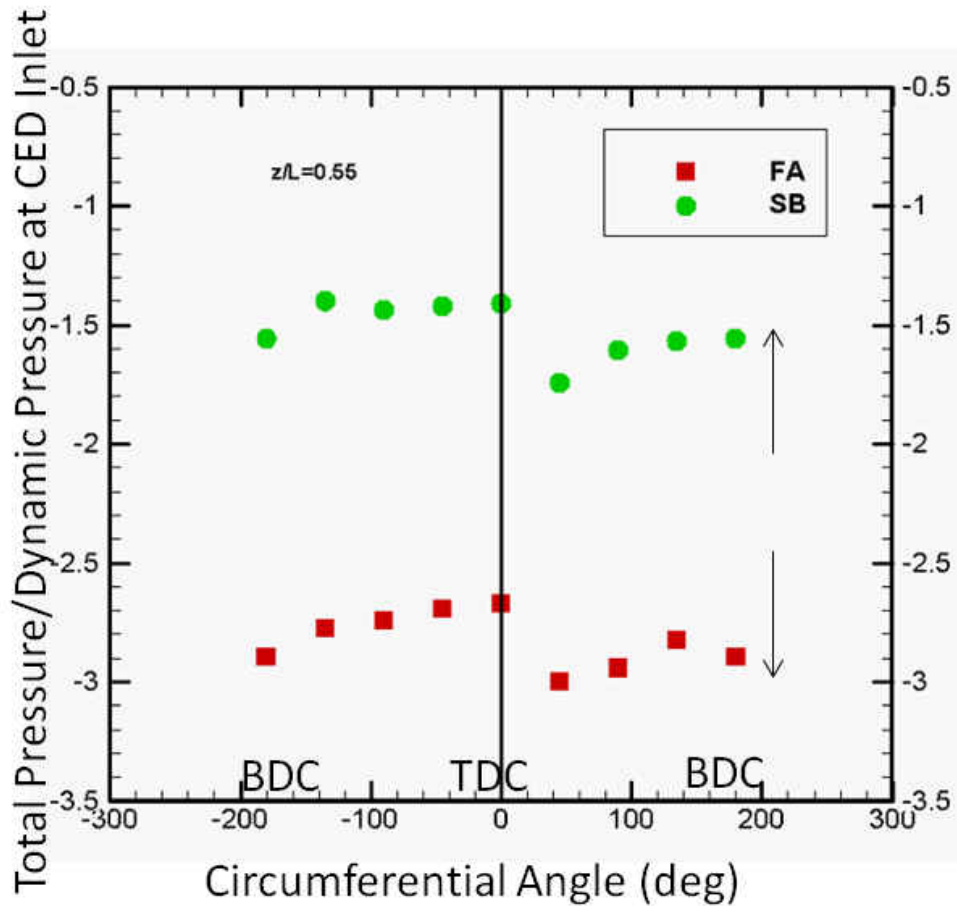


Figure 27: Combustor portal total pressure variation at $z/L = 0.55$

Figure 27 shows the circumferential variation of total pressure normalized by CED inlet dynamic head. The trends are very similar between the two inlet conditions where the lower total pressures are caused by the mounting bracket of the C-stage fuel injection wake region. The total pressure is fairly uniform elsewhere. The offset in magnitudes is a result of the higher pressure drop of the screens used for the FA case and does not reflect a change in MidFrame pressure loss or flow behavior. Total pressures downstream diminish uniformly slightly due to friction in the

annular duct while the deficit from the C-stage mount gets mixed out making the inlet to the combustor quite uniform in total pressure for both inlet conditions.

Figure 28 shows the circumferential and axial pressure coefficients for the combustor portal flow. There is a tendency for higher flow rates near the bottom dead center region of the combustor portal in both inlet cases. The FA case appears to have higher velocities throughout with a lesser absolute pressure coefficient throughout. There is a trend for both of increasing pressure coefficient as the flow nears the diffusion just before the combustor inlet.

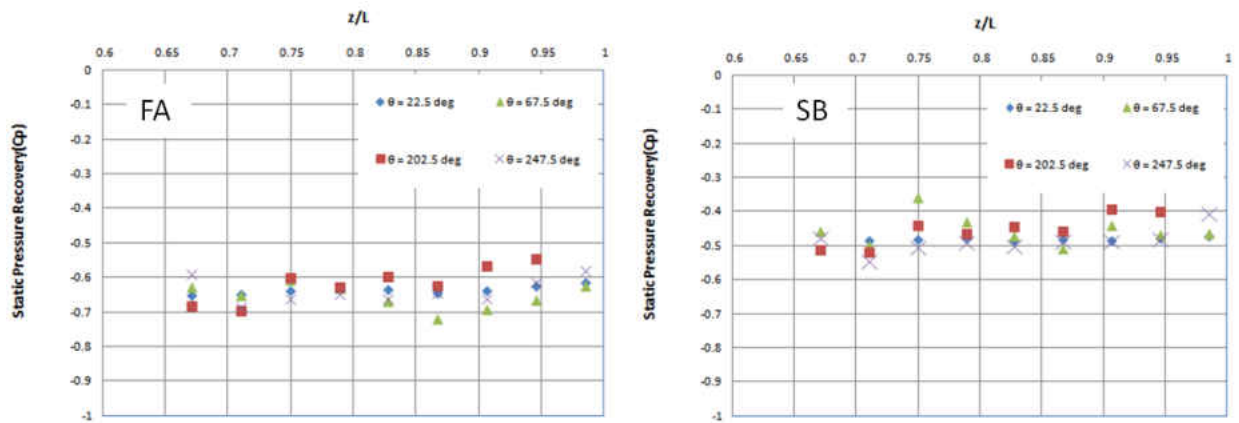


Figure 28: Circumferential and axial pressure coefficient in the combustor portal

Time Accurate Results

The first time accurate data to consider is that of the SB inlet configuration for the CED location microphone and accelerometer shown in Figure 29. The methodology is applied in the sense that the peaks resulting from the coherence between the microphone and accelerometer at this location have been blacked out from the figure since they are deferred for future investigations. After eliminating wall vibrations or fluid-wall coupled frequencies only one peak

is left as a candidate of flow generated unsteadiness. The 100 Hz peak is then passed through the methodology by check uniqueness between inlet conditions. Figure 30 shows the same location for the FA inlet condition. While the 100 HZ does appear to be common between both microphone signals, the peak is also common with the wall vibration in FA case. This defers the peak as potential fluid-wall coupling. What is unique in the FA case is a distinct peak at 10 Hz that is not measured with accelerometer in FA case or the microphone in the SB case. The SB and FA cases each have at least one peak of interest each for further investigation.

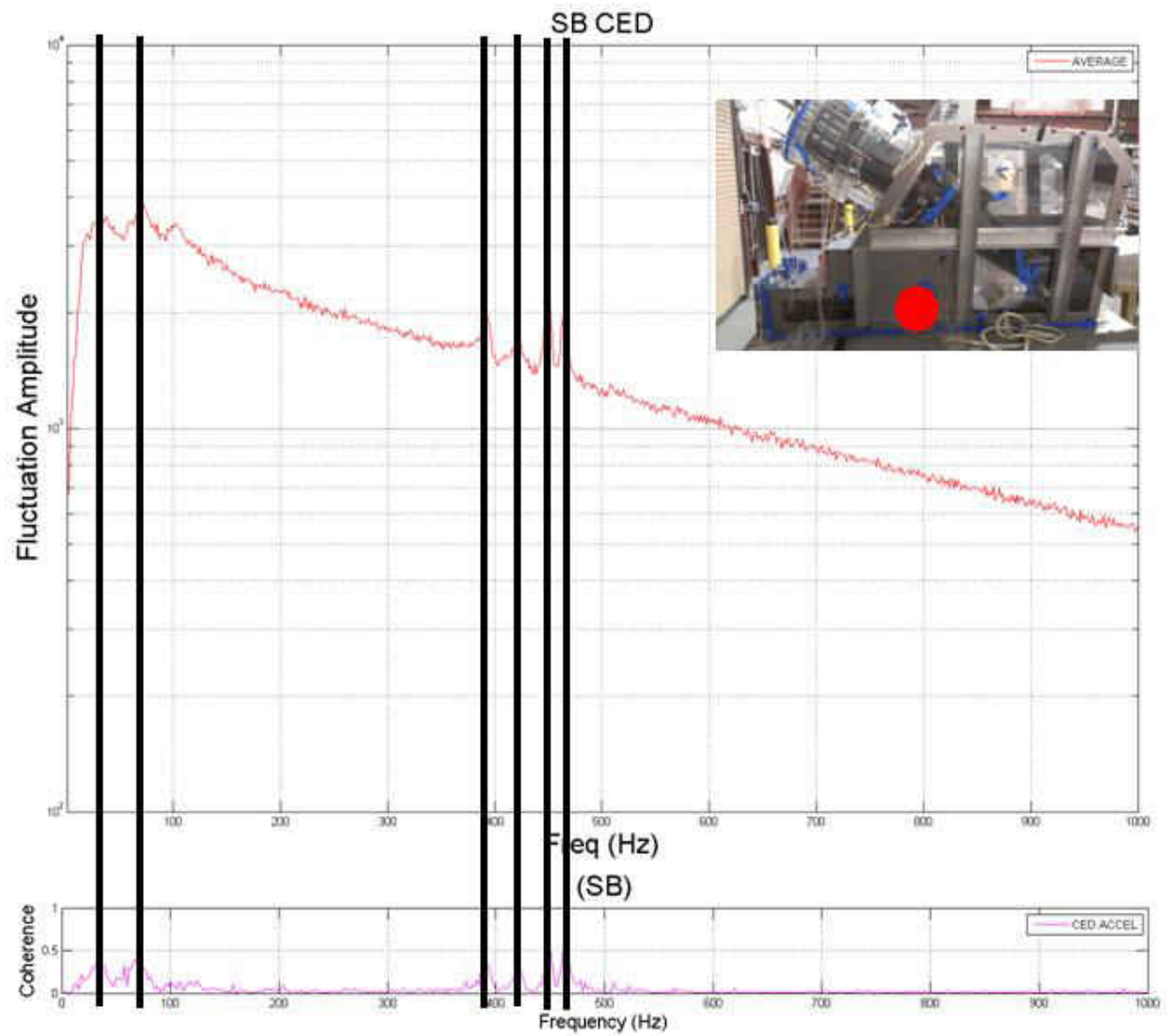


Figure 29: Microphone and mic-accel coherence for CED location SB case

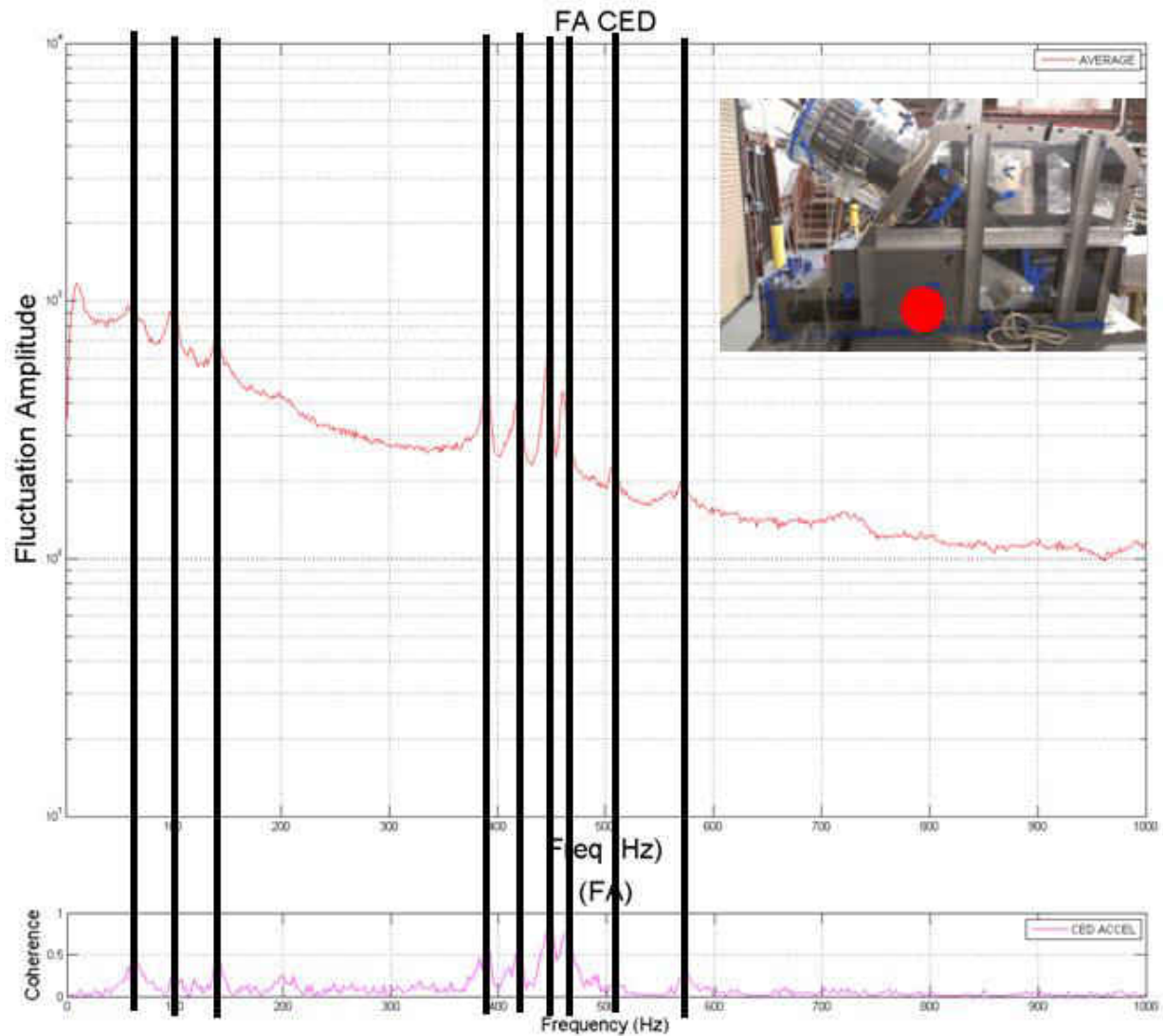


Figure 30: Microphone and mic-accel coherence signal for CED location FA case

Figure 31 shows the microphone and mic-accel coherence signals for the BDC location. Behind the blacked out region one can see that the overall level of unsteadiness is much higher than in the CED region. This is a result of the lower mean velocities and the large amount of geometric obstructions to the flow including the downstream region of the main strut at the CED exit, the transition support (“bullhorn”), and the inlet step into the combustor portal. One caveat

of deferring the common peaks between the accelerometer and microphone is apparent particularly in this location. There are many significant peaks in the microphone signal which may be inducing the same frequency in the wall vibration. These peaks can be shown to lie within potential geometry ranges of frequency based on simplified correlations involving backward facing steps or cylinders in crossflow. Nevertheless, further investigation into these peaks is left for future efforts. A peak can be seen at approximately 10 Hz for this location, whereas at the CED location for the SB case did not appear to share the same peak. It may be concealed by neighboring peaks in the spectra. There are also multiple peaks in the 800-1000Hz range which may or may not be tied with wall vibration. There is potential for these higher registers to be generated from the small features of the supporting structure of the transition. This will require validation with LDV as the location is inaccessible with the current hotwire probe. Figure 32 for the corresponding location of the FA case shows similar behavior with a distinct peak at 10 Hz, some higher register peaks in the 800-1000Hz range (though some are eliminated by the coherence signal), and the rest eliminated as common to the wall vibrations. The 10 Hz peak is of interest since it is appearing in all cases for the two locations thus far.

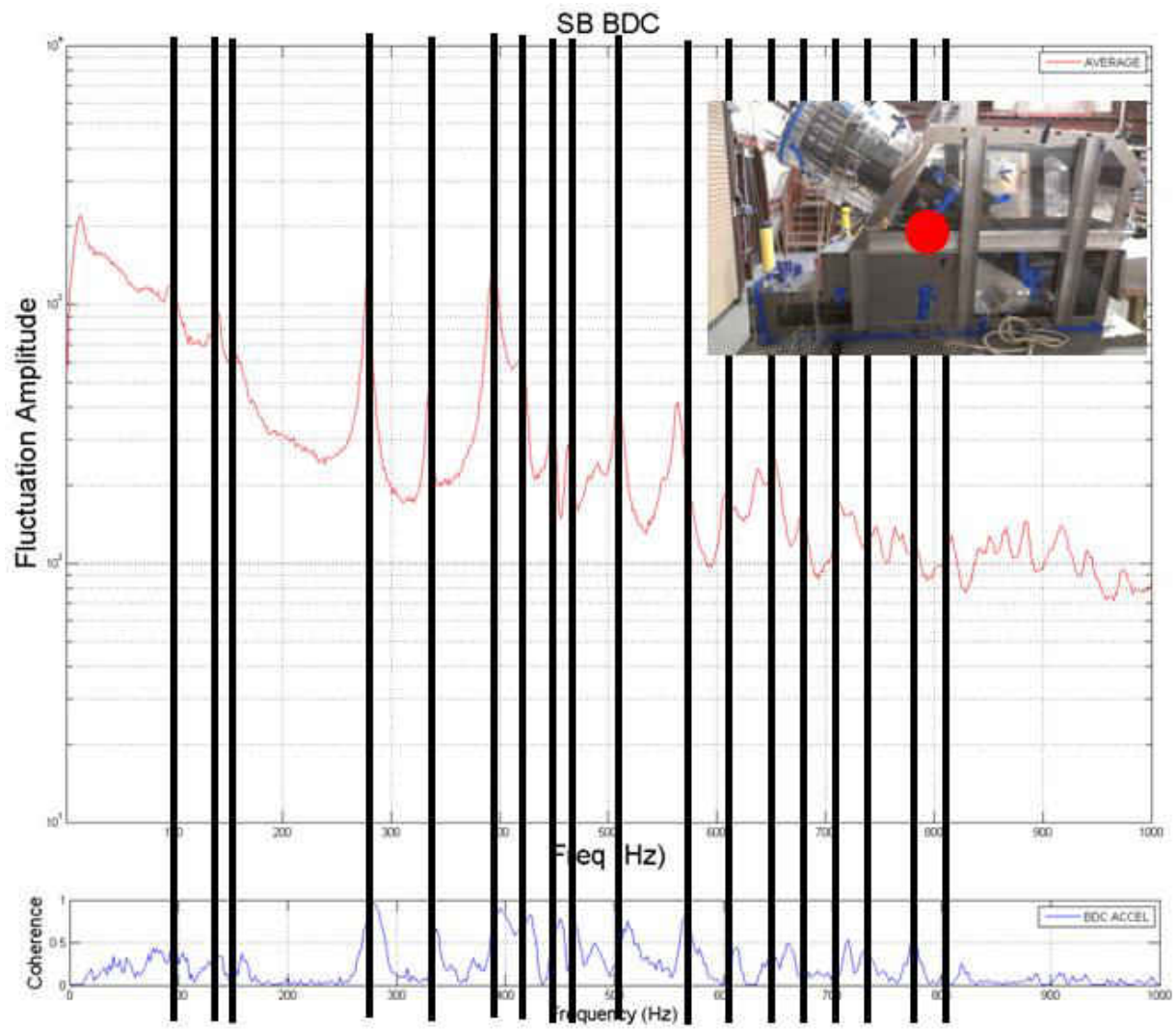


Figure 31: Microphone and mic-accel coherence signal for BDC location SB case

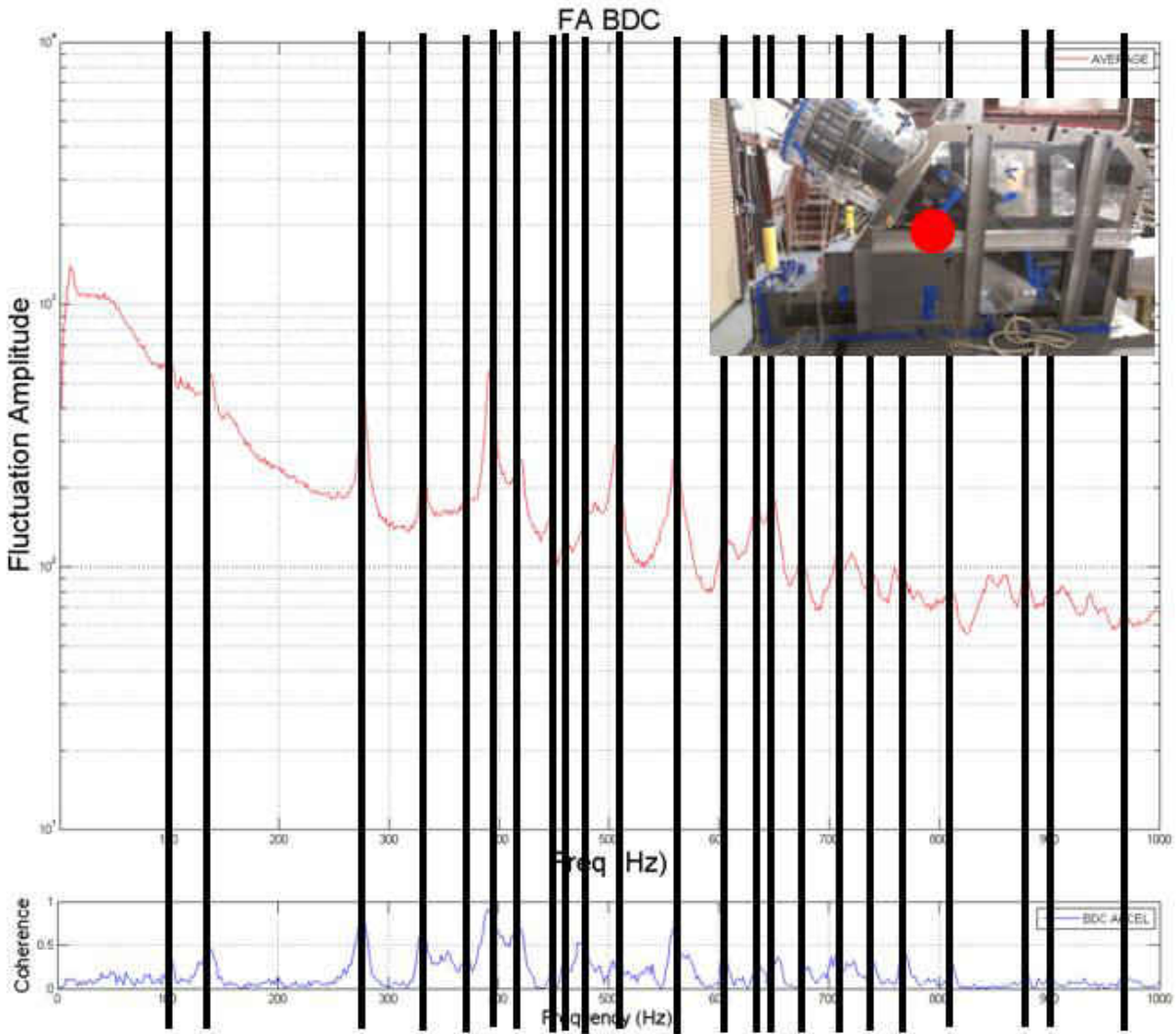


Figure 32: Microphone and mic-accel coherence signal for BDC location FA case

Moving through to the next location for the SB case, Figure 33 shows the signals of the TDC location. This location is very similar to the BDC location with the presence of the 10 Hz peak as well as some of the upper register peaks which are not necessarily eliminated by the coherence signal. Figure 34 shows a different story however as the 10 Hz peak is not as apparent for this inlet condition. Most of the other peaks are eliminated by the coherence signal.

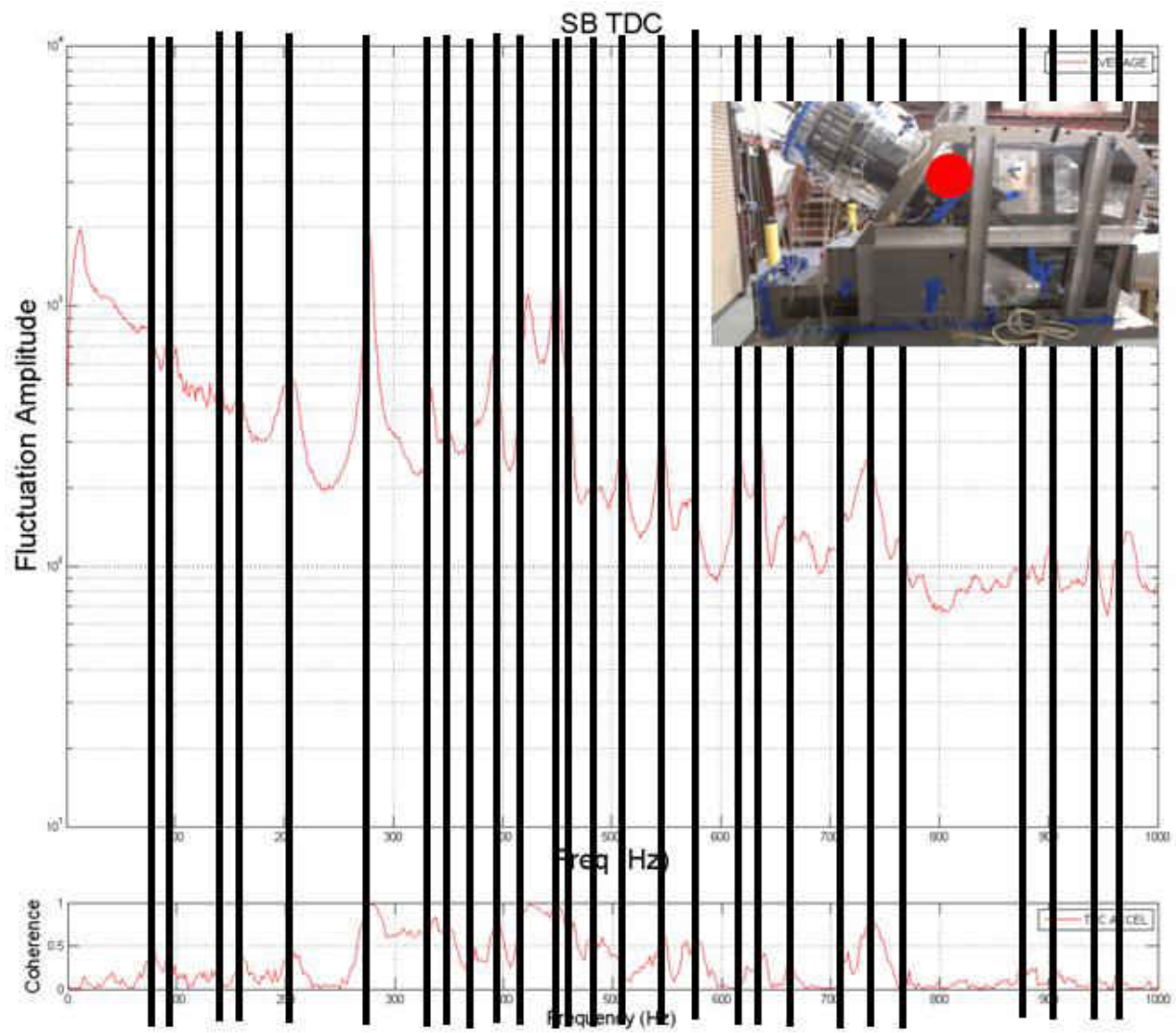


Figure 33: Microphone and mic-accel coherence signal for TDC location SB case

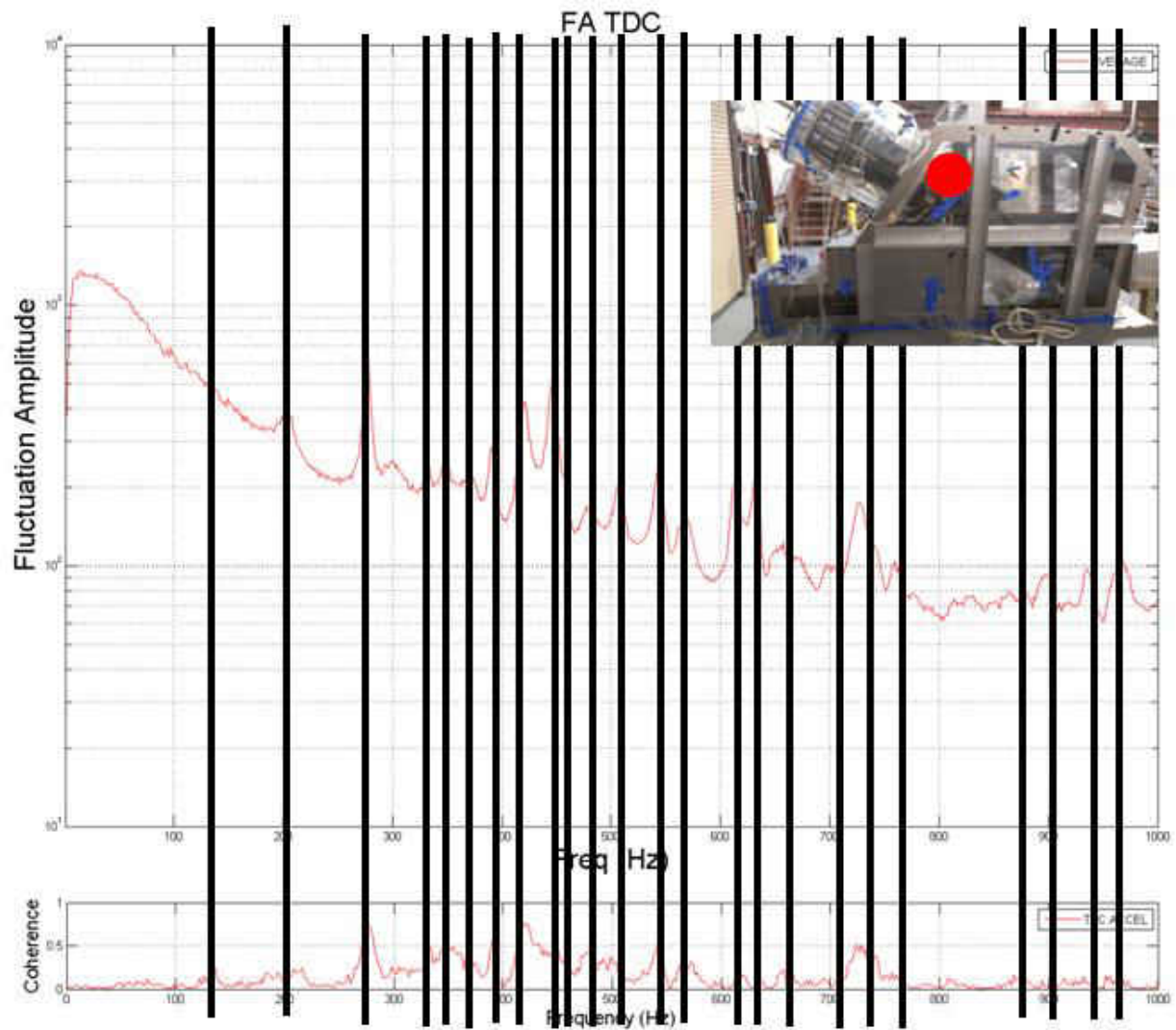


Figure 34: Microphone and mic-accel coherence signal for TDC location FA case

Figure 35 shows the transition location microphone signals for the SB case. One would expect to see the transition wake frequency in the signal as it most represents a cylinder in cross flow of all locations in the domain. The predicted frequency would lie between 20-40 Hz. The microphone signal shows a prominent 10 Hz peak as well as a smaller broader peak at approximately 30 Hz which is suspected to be the transition wake unsteadiness. Figure 36 shows

the same location for the FA case. The 10 Hz is still apparent but the 30 Hz peak is not prominent. This may be a result of the lower average velocity impinging on the transition from the fully attached CED outlet causing a shift of the transition wake towards the already apparent 10 Hz peak. Also evident in the FA case is a 210 Hz peak which is not eliminated from the coherence as was the case in the SB case. This 210 Hz peak appears to be common to the TDC and BDC locations as well. Later in the results, coherence between microphone locations will be used to determine where the peaks are most prominent in effort to locate the general location of the source.

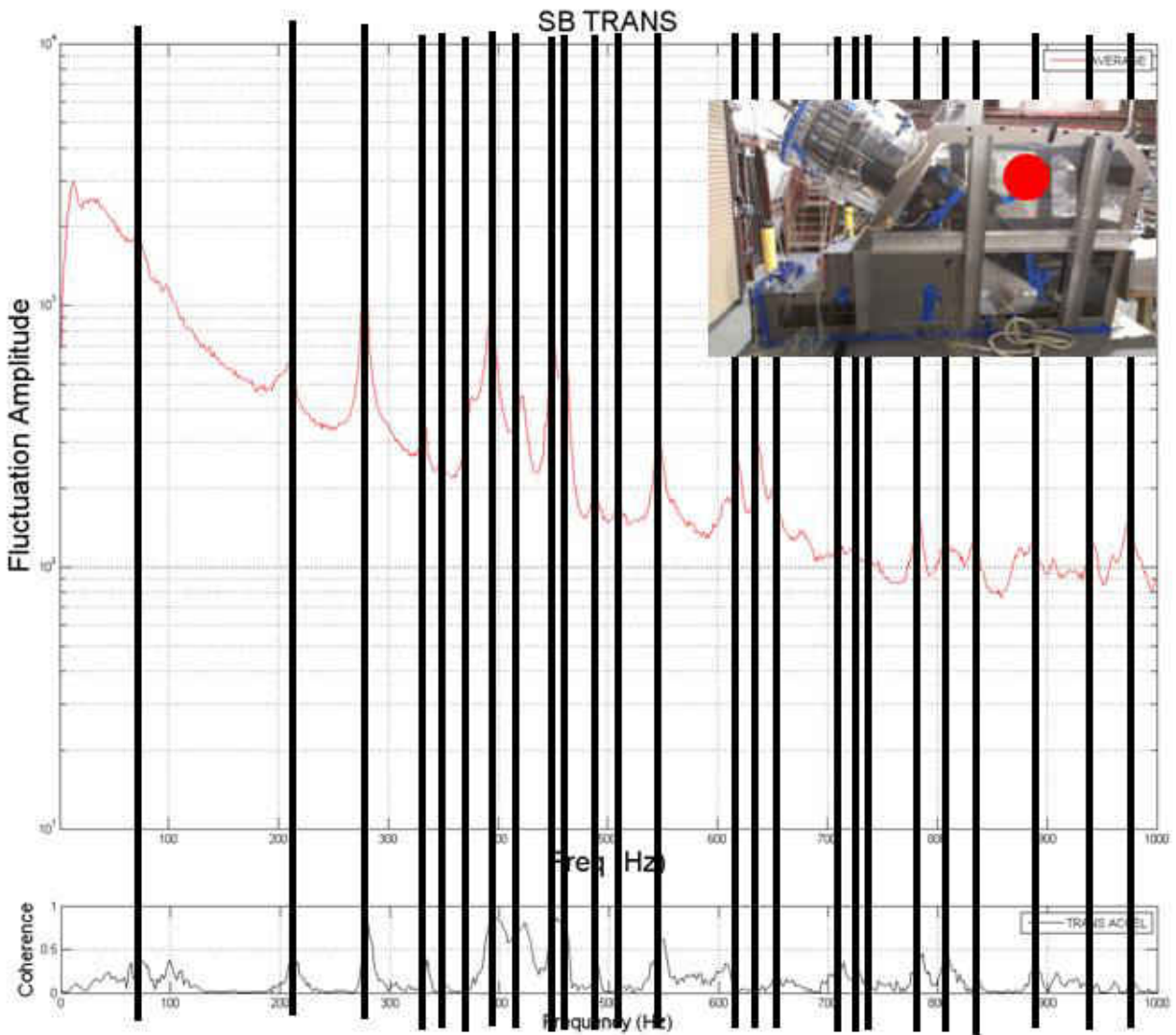


Figure 35: Microphone and mic-accel coherence signal for transition location SB case

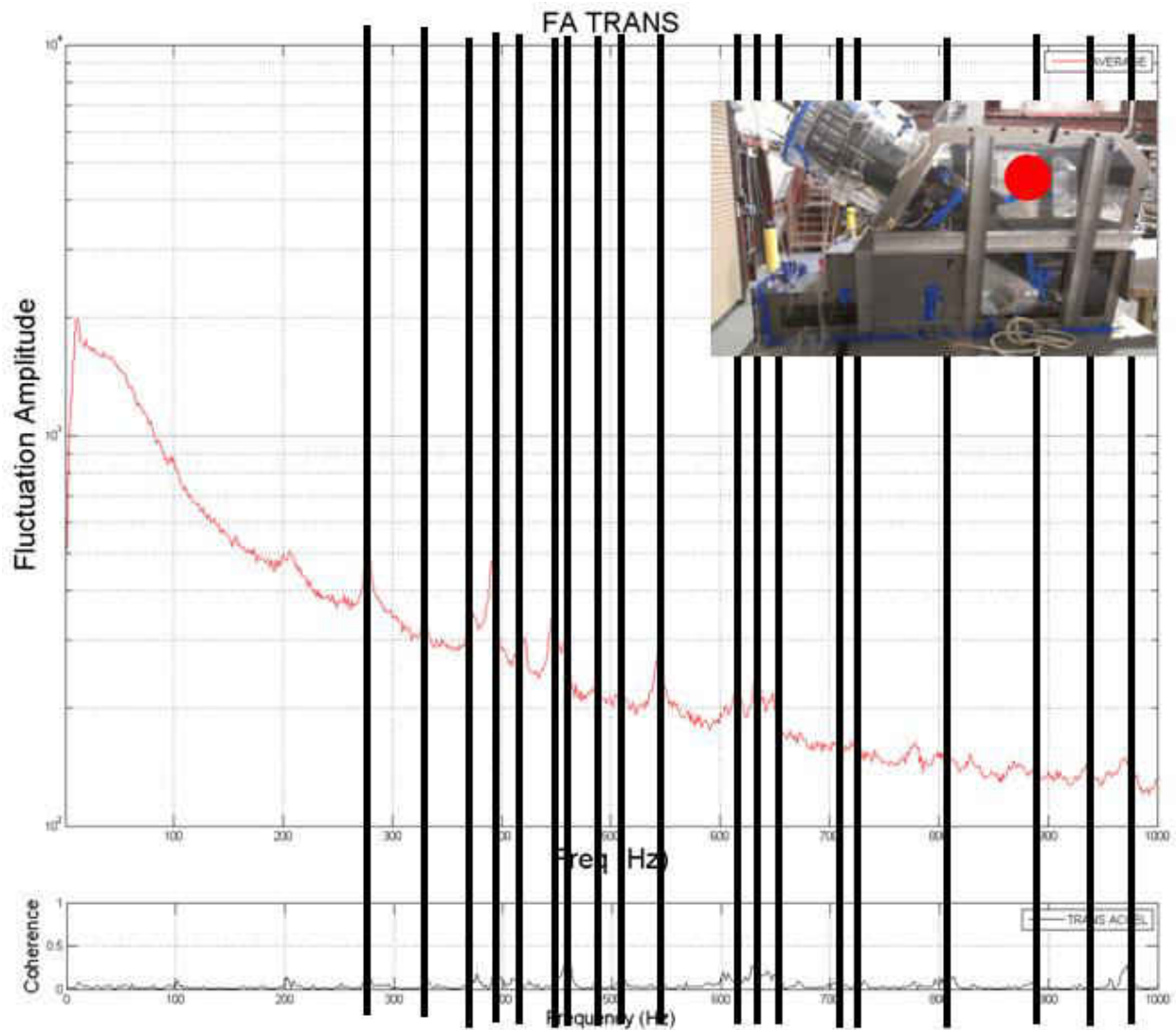


Figure 36: Microphone and mic-accel coherence signal for transition location FA case

The last microphone location to be measured is the tophat region. Figure 37 shows this location for the SB case. The ubiquitous 10 Hz peak is still present with no corresponding signal in the accelerometer to eliminate it as potential unsteadiness. Also remaining after the elimination process is a smaller peak at 60 Hz and 550 Hz. Figure 38 shows the same location for the FA case. Here the 10 Hz is still apparent, a very small indication of the 60 Hz peak, and a

100 Hz peak are remaining after elimination. The 550 Hz peak is also still present. All considered the only differences between the two inlet conditions at this location are the prominence of the 60 Hz peak and the fact that the 100 Hz peak is common with the accelerometer in the SB case but not in the FA case.

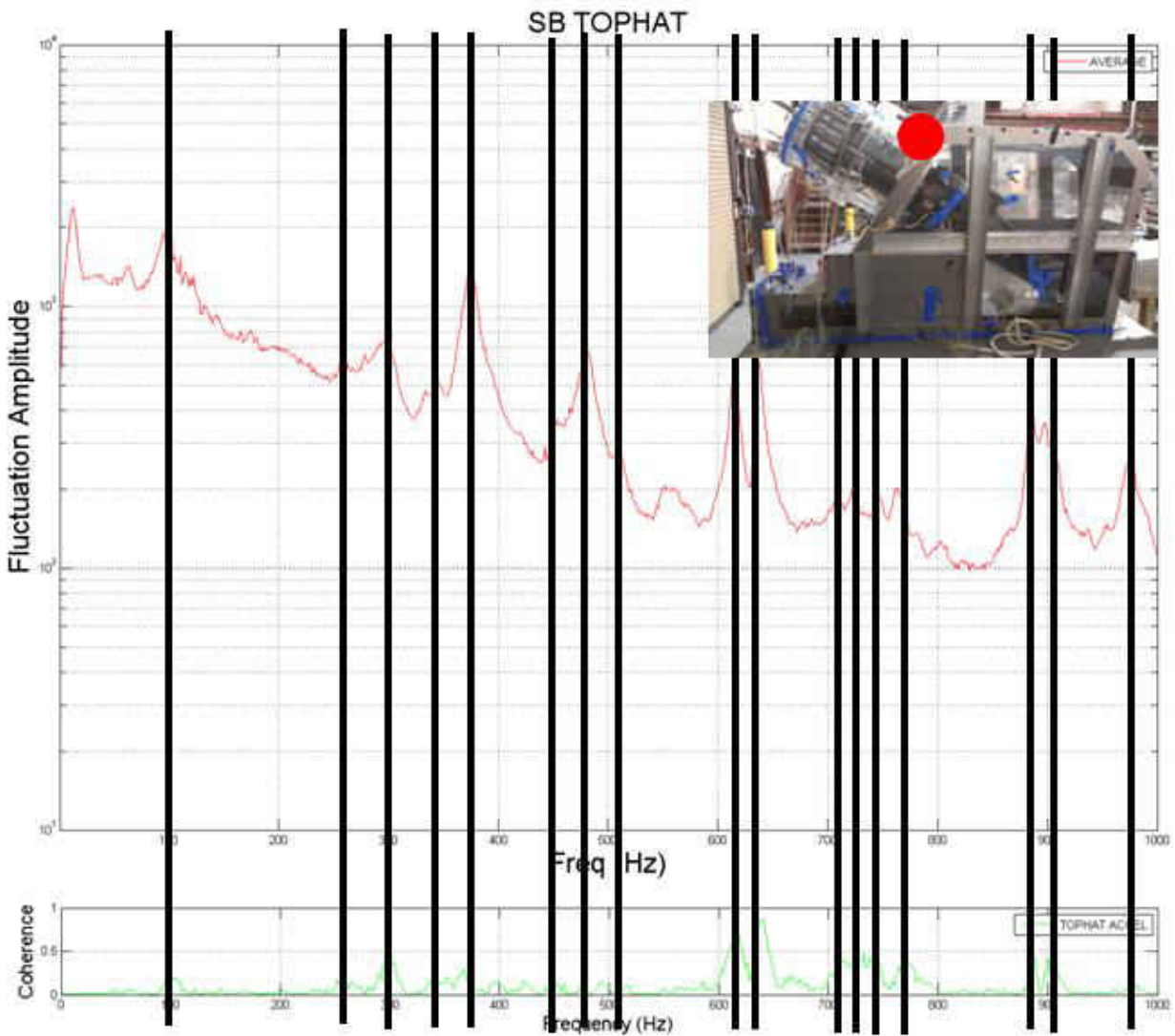


Figure 37: Microphone and mic-accel coherence signal for top hat location SB case

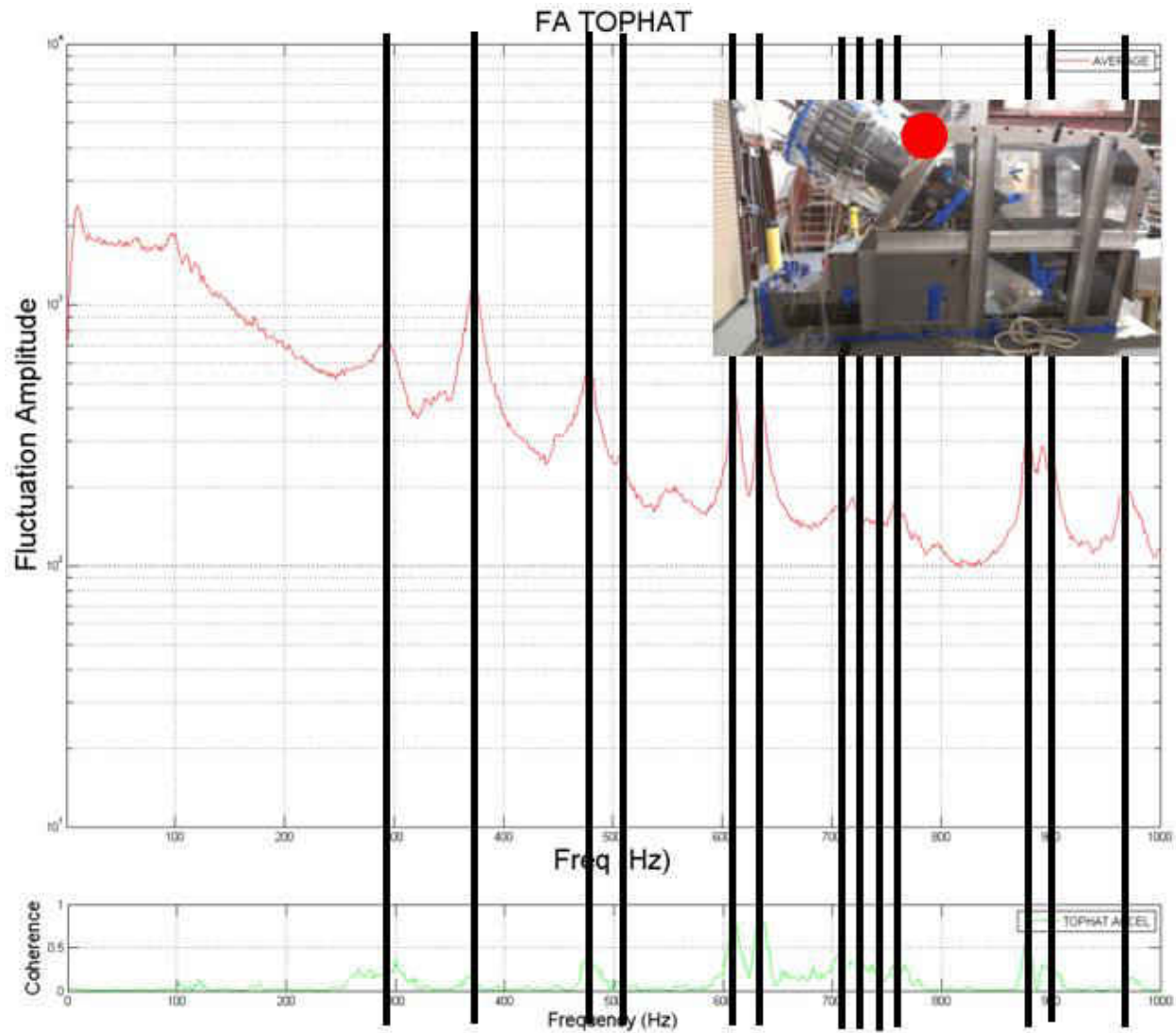


Figure 38: Microphone and mic-accel coherence signal for top hat location FA case

The resulting peaks from the elimination process are compiled and investigated for overlap between locations. The coherence function can be applied between microphone locations which can aid in determining the most probable source of unsteadiness as opposed to a convective location which indicates the same frequency. Figure 39 shows the coherence between the CED microphone and other locations for the SB inlet condition. Peaks of interest can be

traced through the domain using the relative magnitude of coherence as an indicator of relative strength of unsteadiness. The 10 Hz peak can be seen to be common between CED and all locations, least of which is the CED-Transition pair where the coherence is somewhat less than the other pairs. The 100 Hz peak at the SB CED location appears to be unique to that location as it does not appear in the coherence between any other location. The remaining peaks were associated with the wall vibrations, though they are not indicated in Figure 39. Figure 40 offers the same treatment for the FA inlet condition. The 10 Hz peak shows similar behavior in this case where it is common for all locations and less so for the CED-Transition pair. The small peak at 720 Hz in the FA case CED location appears also in the BDC location and less so in the TDC location. This supports the conjecture that it is related to the transition underside support mount since it is stronger for the BDC location. Also of note is the fact that at the BDC location this peak is common with the wall vibration but not so in the CED location. A potential cause is the CED microphone picking up remnants of the pressure fluctuation which is generated downstream. This exhibits the difficulty in separating wall vibration and flow unsteadiness particularly where a highly probable and predictable frequency is picked up in the wall mounted accelerometer. The 10 Hz peak is difficult to isolate for validation with hotwire measurements as it appears throughout the domain while not appearing in the wall vibrations. This could indicate some common bulk unsteadiness related to the aft recirculation region which exists for all inlet conditions.

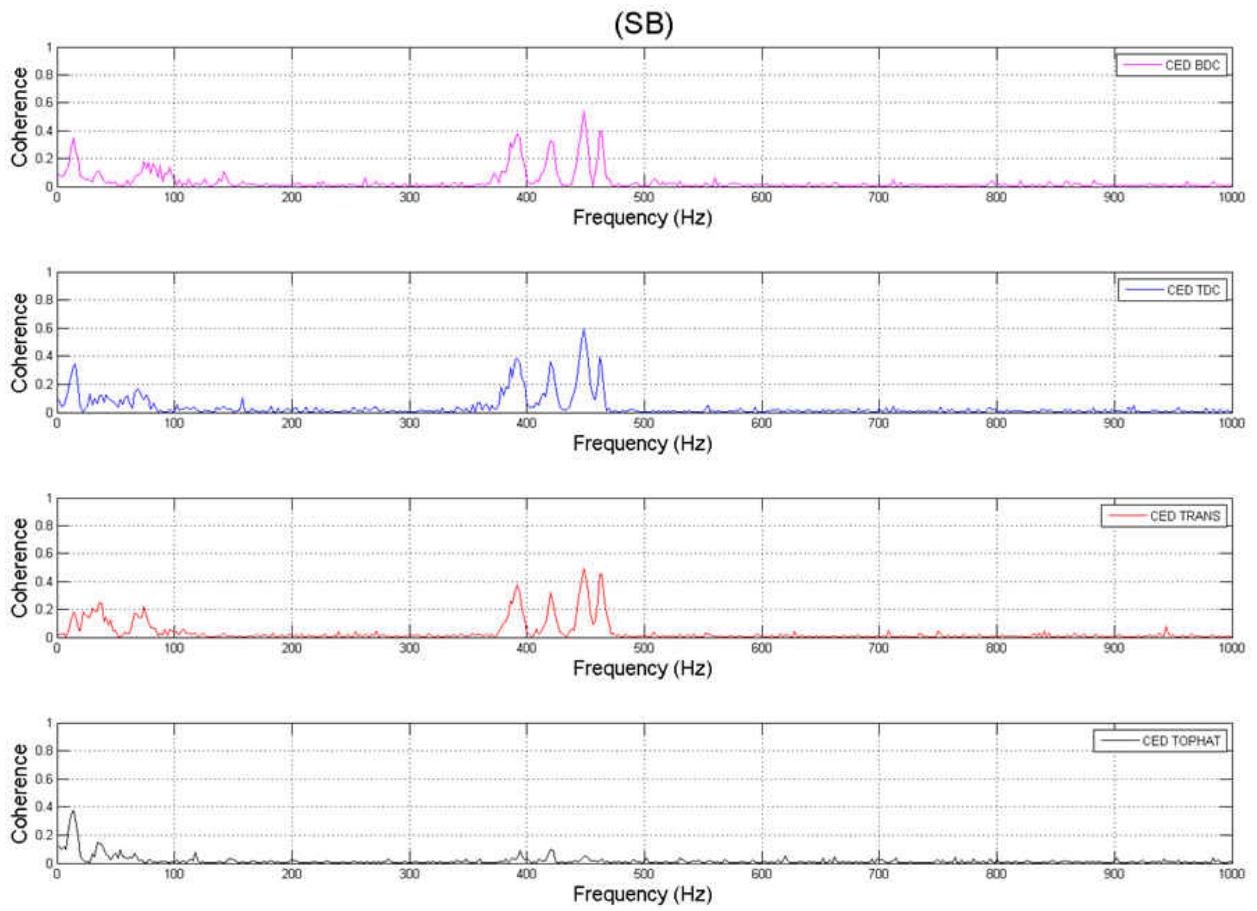


Figure 39: Coherence between CED and other microphone locations for SB case

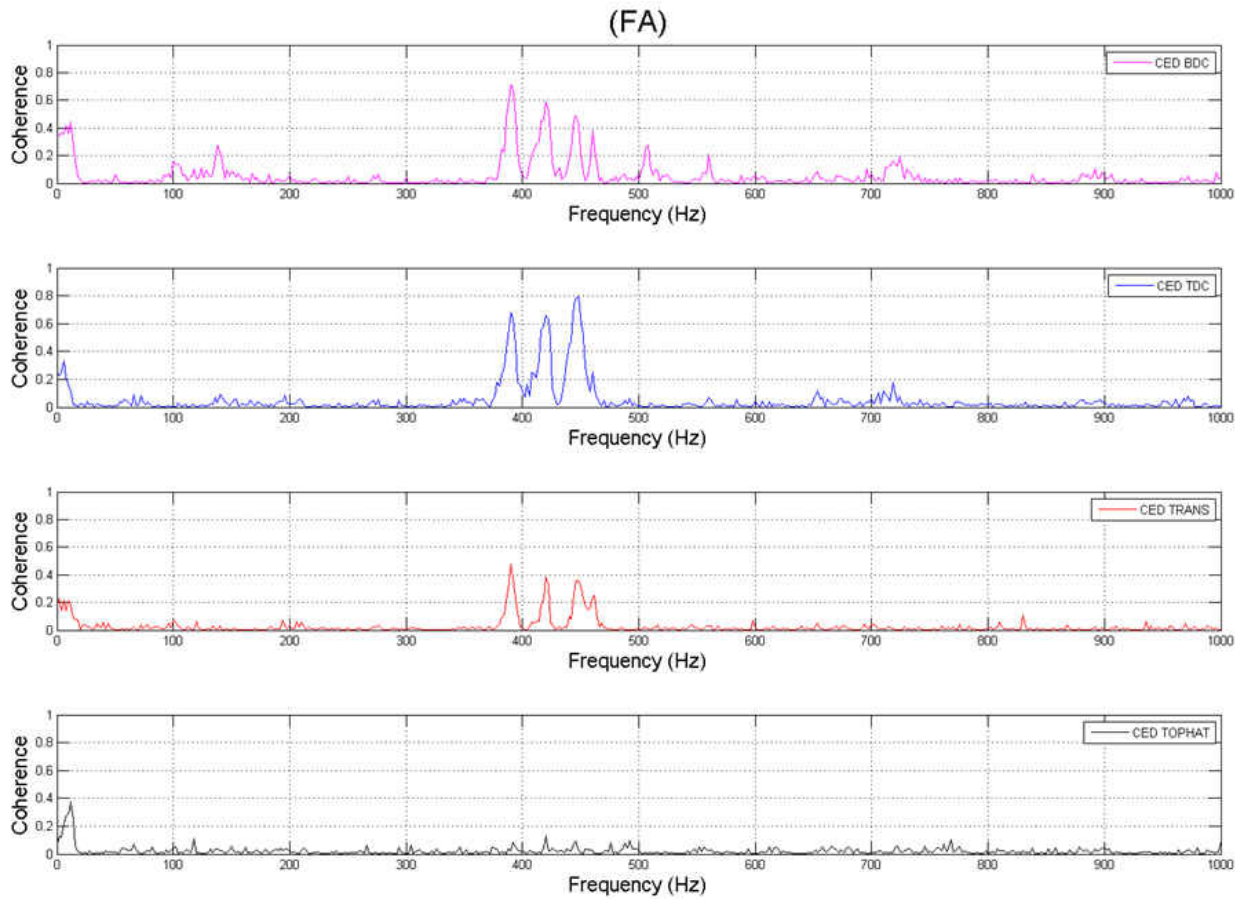


Figure 40: Coherence between CED and other microphone locations for FA case

Next the BDC location’s significant peaks are checked amongst other locations. Figure 41 shows the coherence between the BDC and other locations for the SB inlet condition. As expected there is strong coherence at the 10 Hz peak except with the transition location. The only other peaks of interest at this point in that SB BDC case are the higher frequencies in the 800-1000Hz. From Figure 41 we can see that these are mostly localized to the combustor portal inlet region with strong coherence between BDC and TDC for these ranges and less so for the BDC-Top hat pair. Figure 42 shows the same treatment for the FA inlet condition. Similar behavior of the 10 Hz peak is seen. Similar to the SB case the BDC-TDC pair has high coherence throughout

due to their proximity. The remaining peaks are eliminated in the coherence between the accelerometer and microphone at the BDC location and are outside the scope of the present discussion.

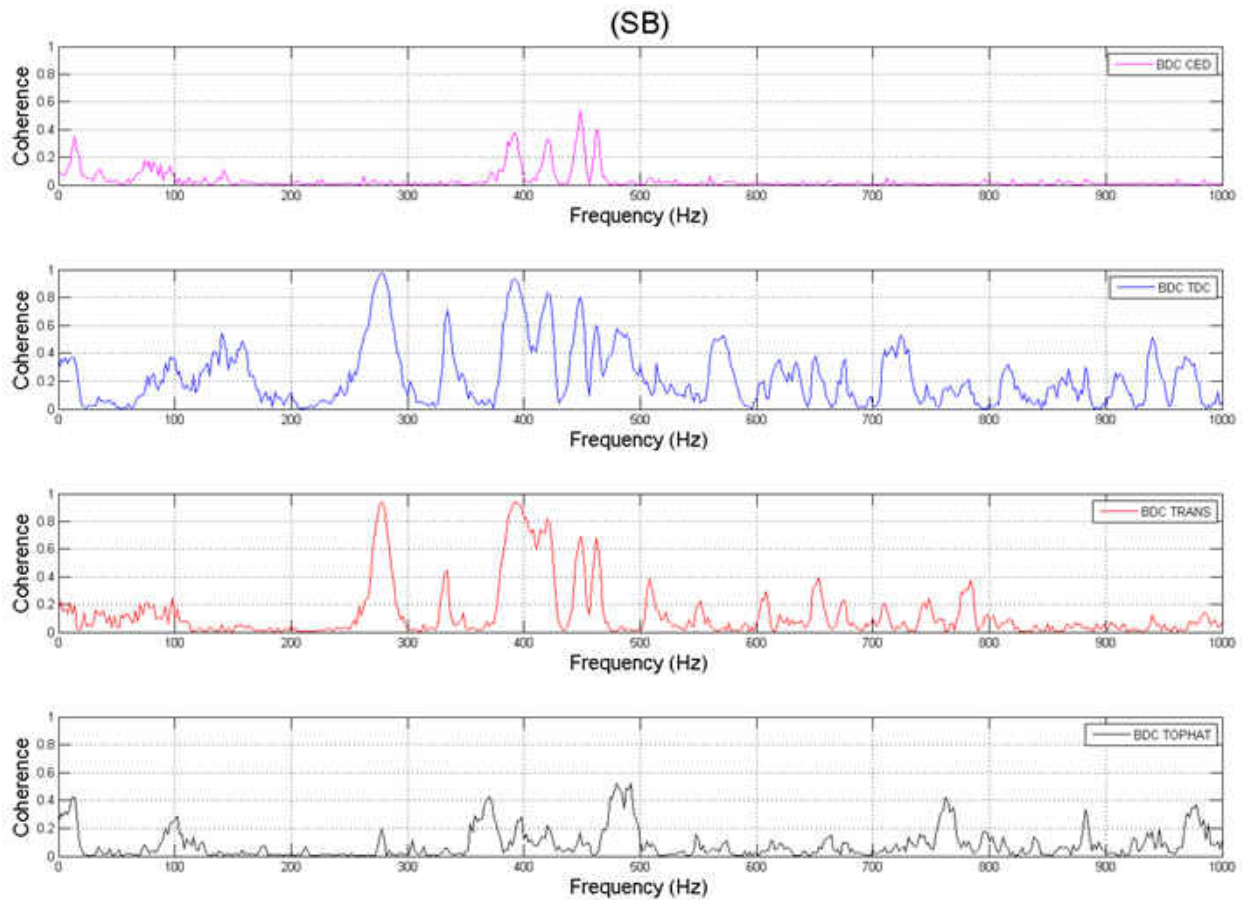


Figure 41: Coherence between BDC and other microphone locations for SB case

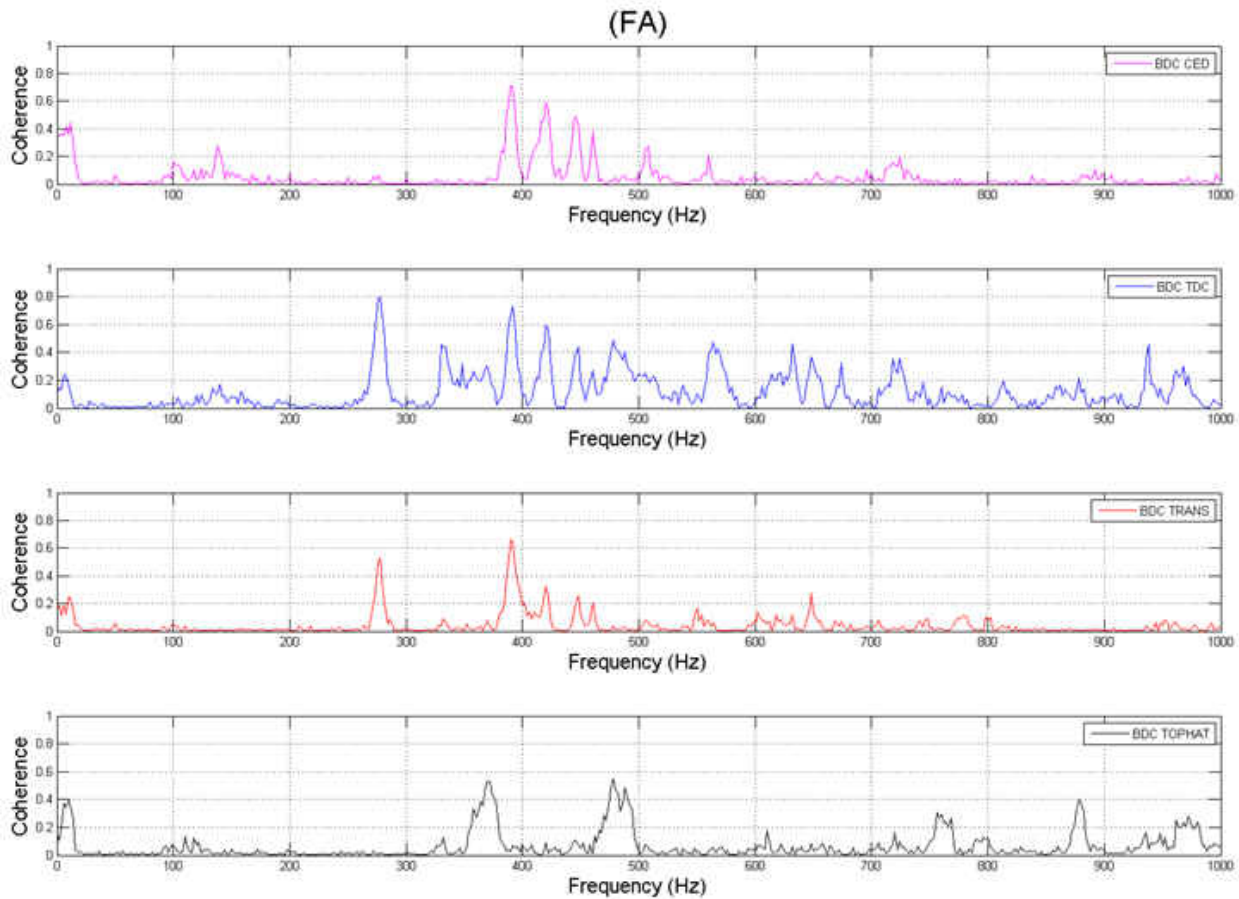


Figure 42: Coherence between BDC and other microphone locations for FA case

The next source location is the TDC location. Figure 43 shows the coherence between the TDC and other microphone s for the SB case. The 10 Hz peak is common in all locations while the coherence between the TDC-Transition pair is slightly stronger than was seen in the BDC-Transition pair indicating that the source of this signal may be closer to the upper portion of the domain for this case. All other peaks are eliminated in the accelerometer-microphone coherence for this location. Figure 44 shows the same result for the FA case. Even though the 10 Hz peak is not distinct in the original microphone signal for the TDC location FA case, the coherence shows that this frequency is common in all locations still.

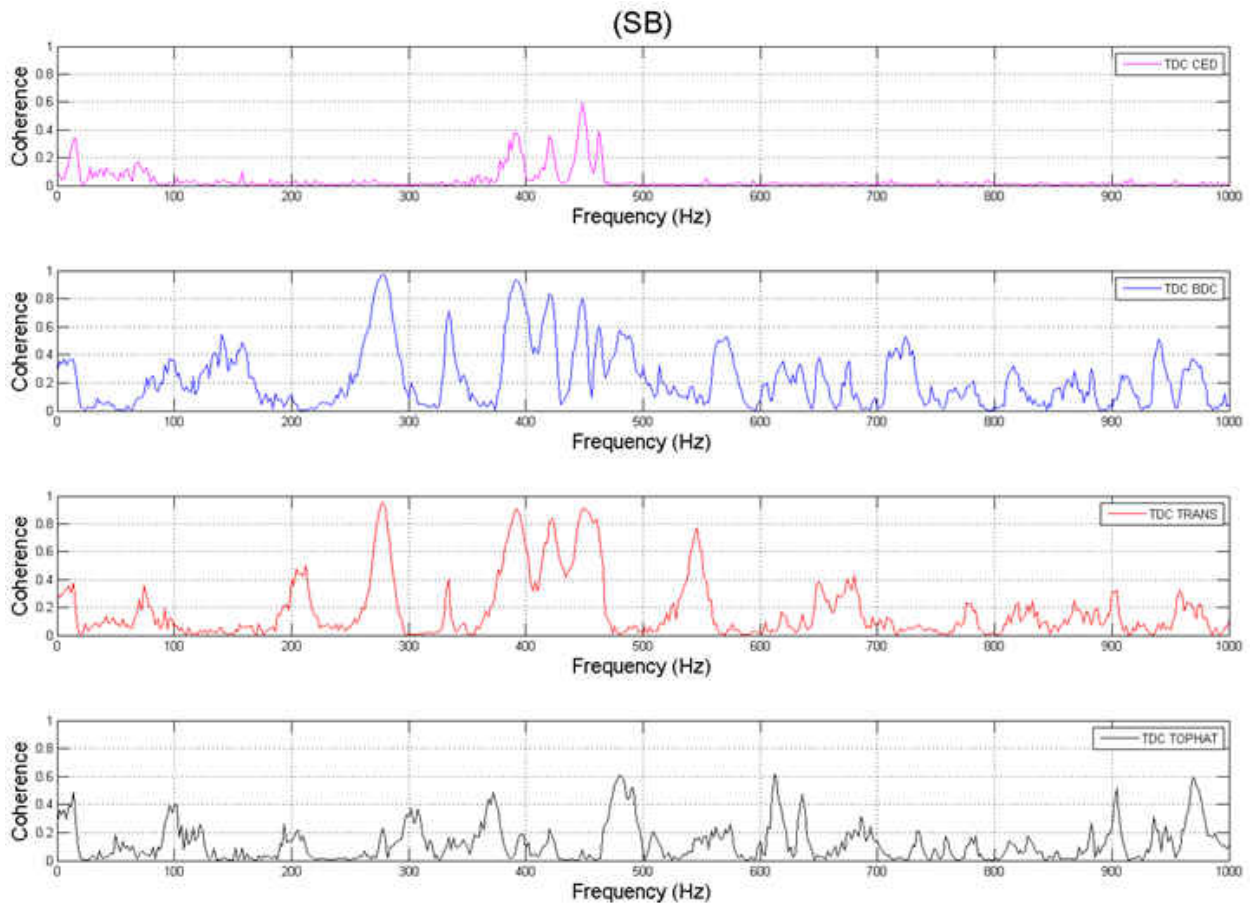


Figure 43: Coherence between TDC and other microphone locations for SB case

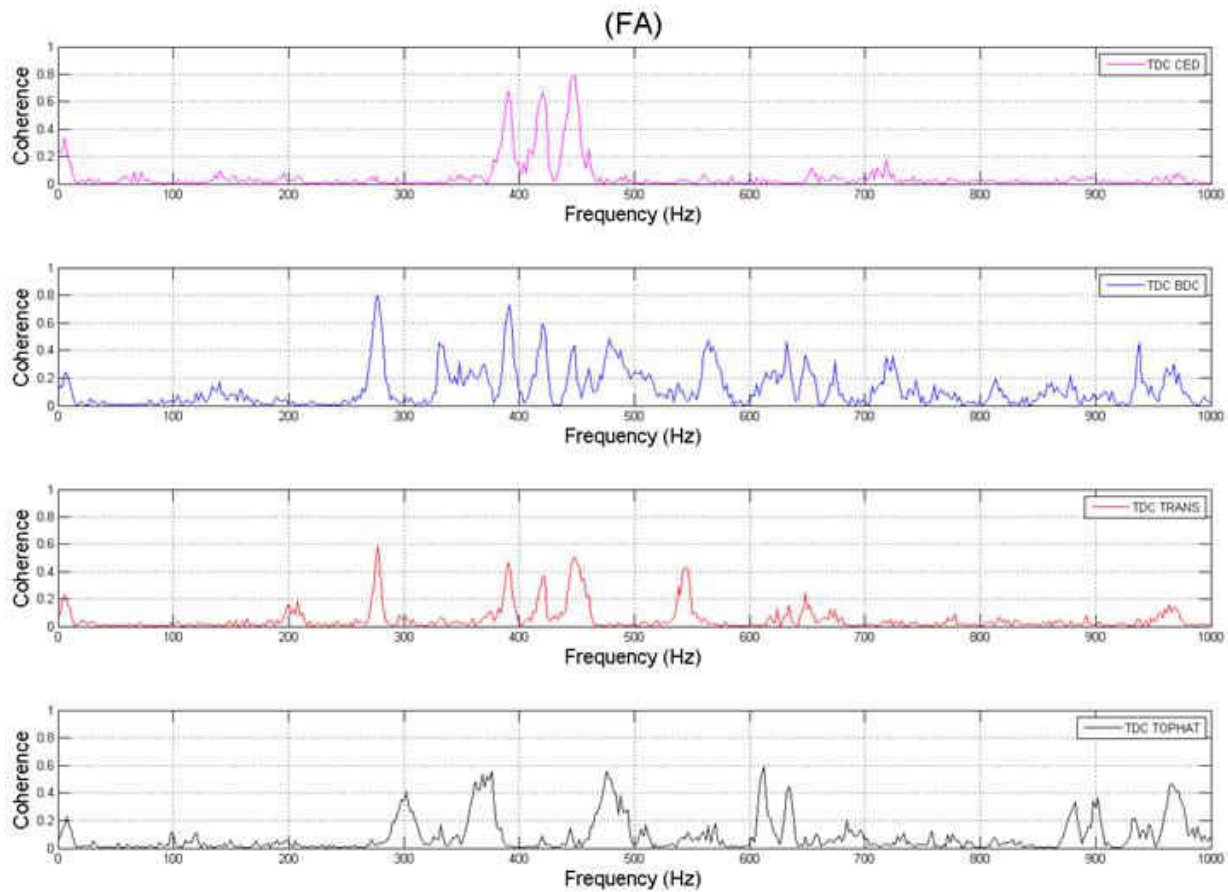


Figure 44: Coherence between TDC and other microphone locations for FA case

The next location is the transition microphone. Figure 45 shows the transition microphone coherence with other locations for the SB case. The 10 Hz peak is not so apparent in the coherence signal with the exception of the Transition-top hat pair. All other peaks were eliminated from the current investigation. Figure 46 shows the same treatment for the FA case. The 10 Hz appears slightly cleaner in this case. The 210 Hz peak which was not eliminated in the original FA Transition microphone signal is only seen to be common with the TDC location where it was common with the accelerometer signal. It is probable that the flow unsteadiness near the BDC location is detected by the transition microphone while the induced wall vibration

is not. The verification of this conjecture requires the detailed analysis of fluid-wall coupled oscillations which will be the focus of the next fiscal year's work.

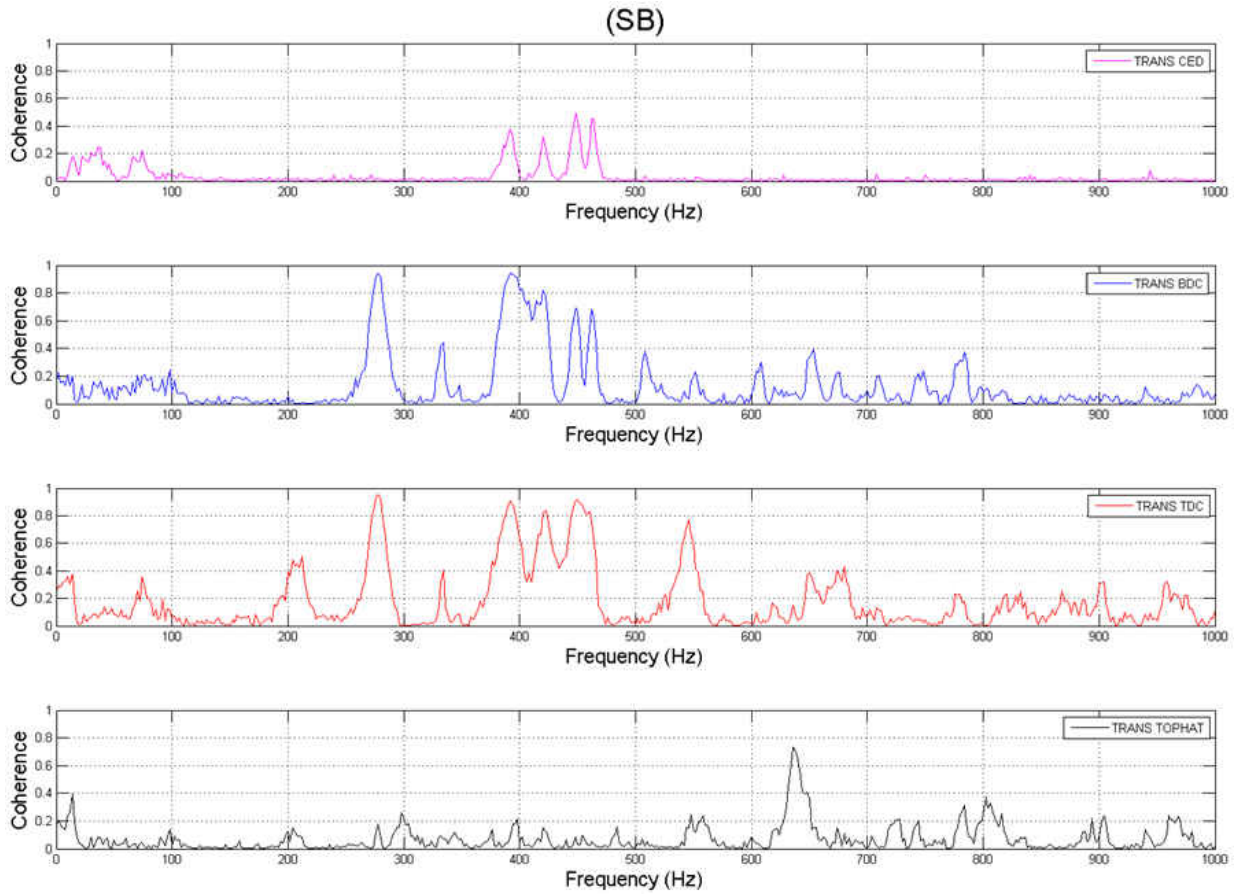


Figure 45: Coherence between transition and other microphone locations for SB case

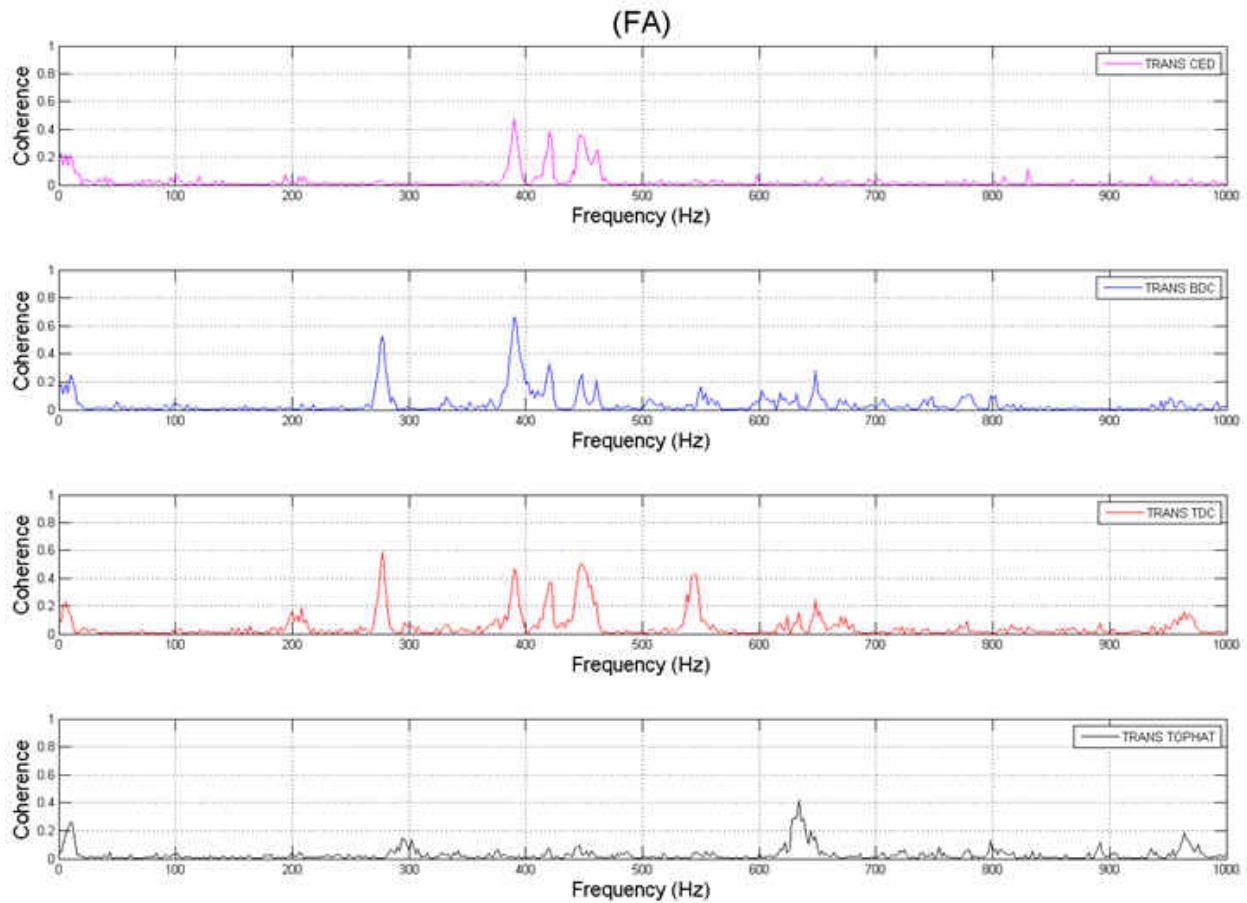


Figure 46: Coherence between transition and other microphone locations for FA case

The last location is the top hat microphone location and is shown for the SB case in Figure 47. The 10 Hz is of course still apparent throughout while there appears to be some overlap at 60 Hz between the top hat and TDC locations. The 550 Hz appears in both the Transition and TDC locations in addition to the top hat location. This would suggest that the source is in the upper most region of the rig. Figure 48 shows the same treatment of the FA case. The smaller 60 Hz peak in the FA microphone signal does not appear in any other location. The same is true for the 100 Hz peak which does not appear to be significant in any of the coherence

pairs. The coherence at the 550 HZ peak is much less for the TDC-top hat pair and not apparent for the Transition-top hat pair.

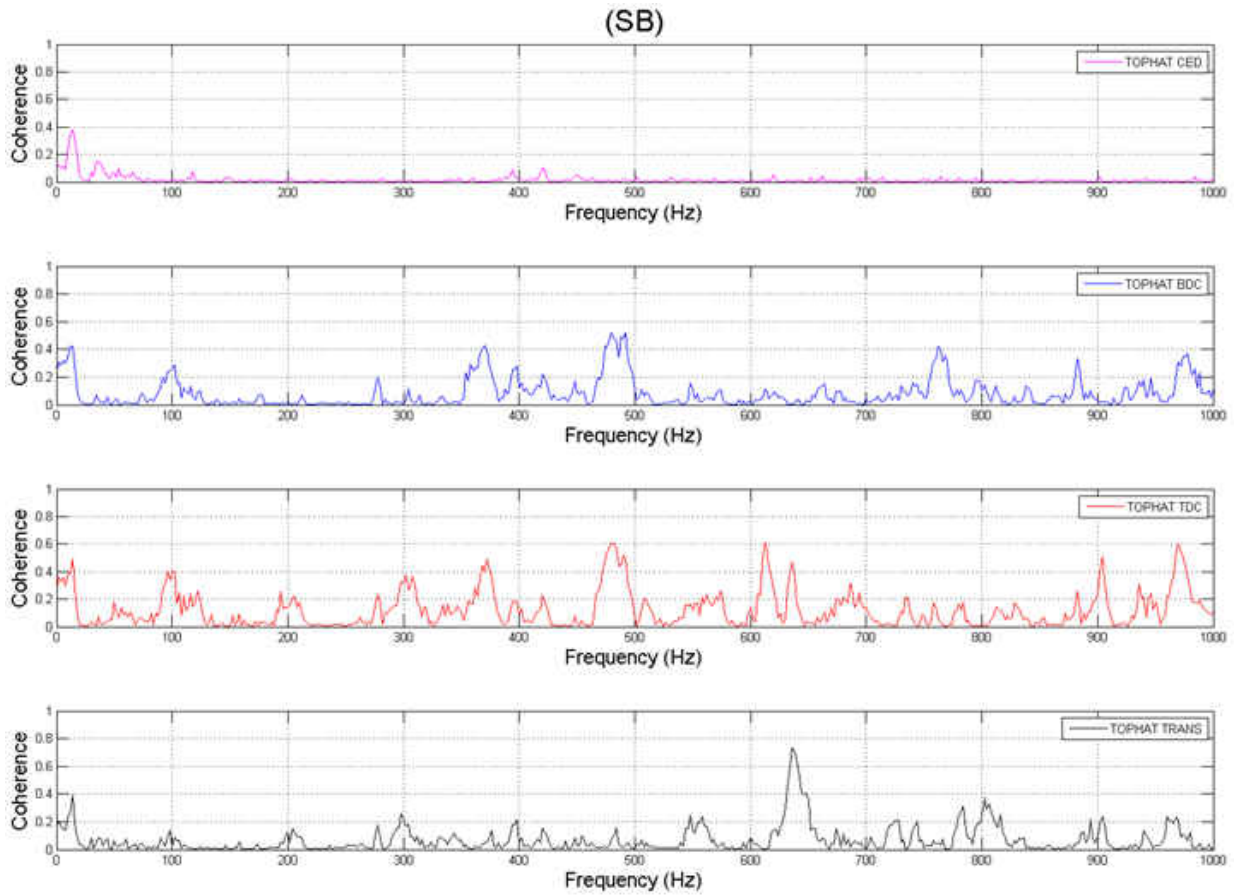


Figure 47: Coherence between top hat and other microphone locations for SB case

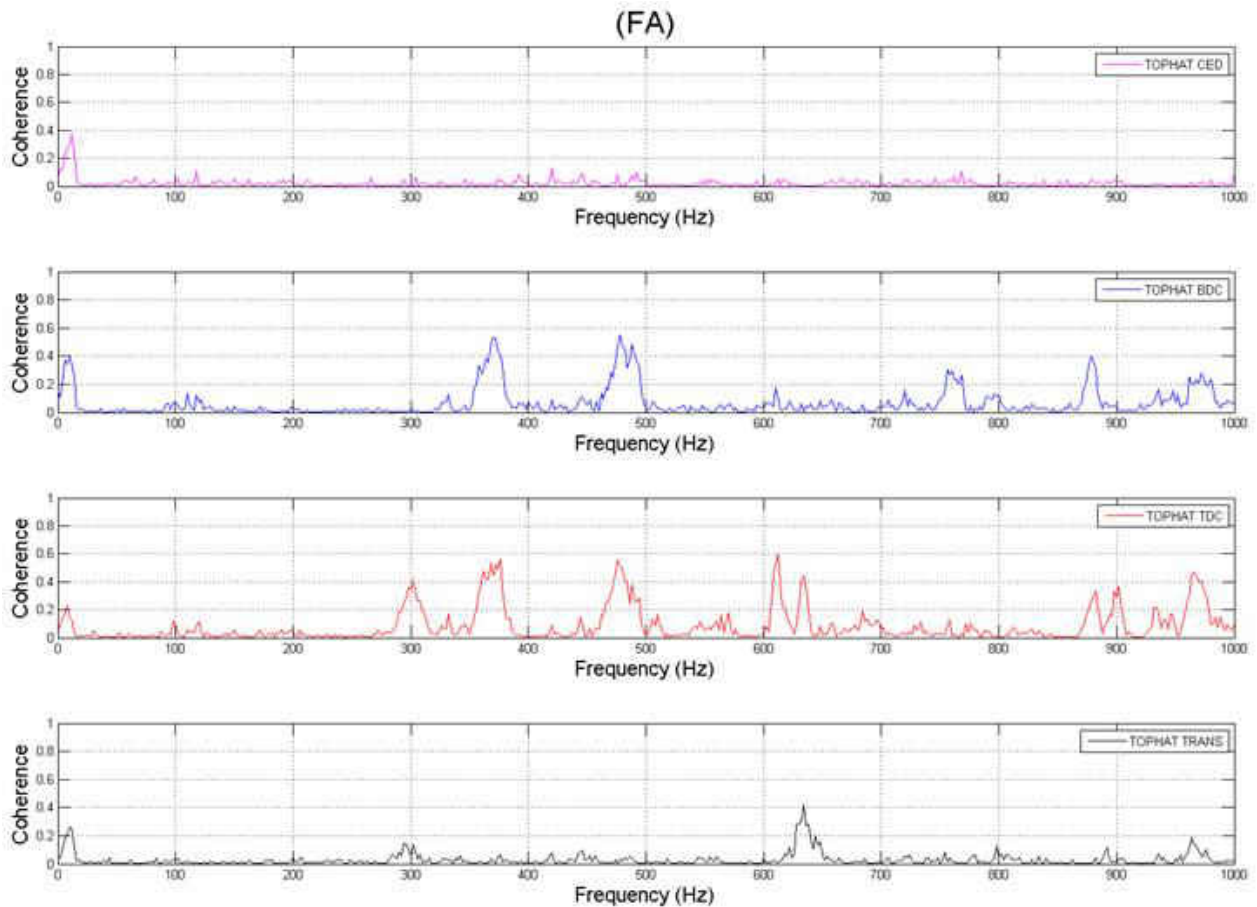


Figure 48: Coherence between top hat and other microphone locations for FA case

The hotwire wire anemometry measurements were used to investigate several of the most likely candidates for flow unsteadiness including the backward facing step (BFS) of the bottom wall immediately after the CED exit, the transition wake region, and the c-stage fuel injection ring in the combustor portal. Figure 49 shows the FFT for the suspected shear layer of the BFS. No distinct unsteadiness was detected for any of the locations in the region immediately downstream of the BFS. This may be a result of the fact that the flow is already turning upwards towards the combustor portal as opposed to a standard BFS geometry where the flow reattaches downstream.

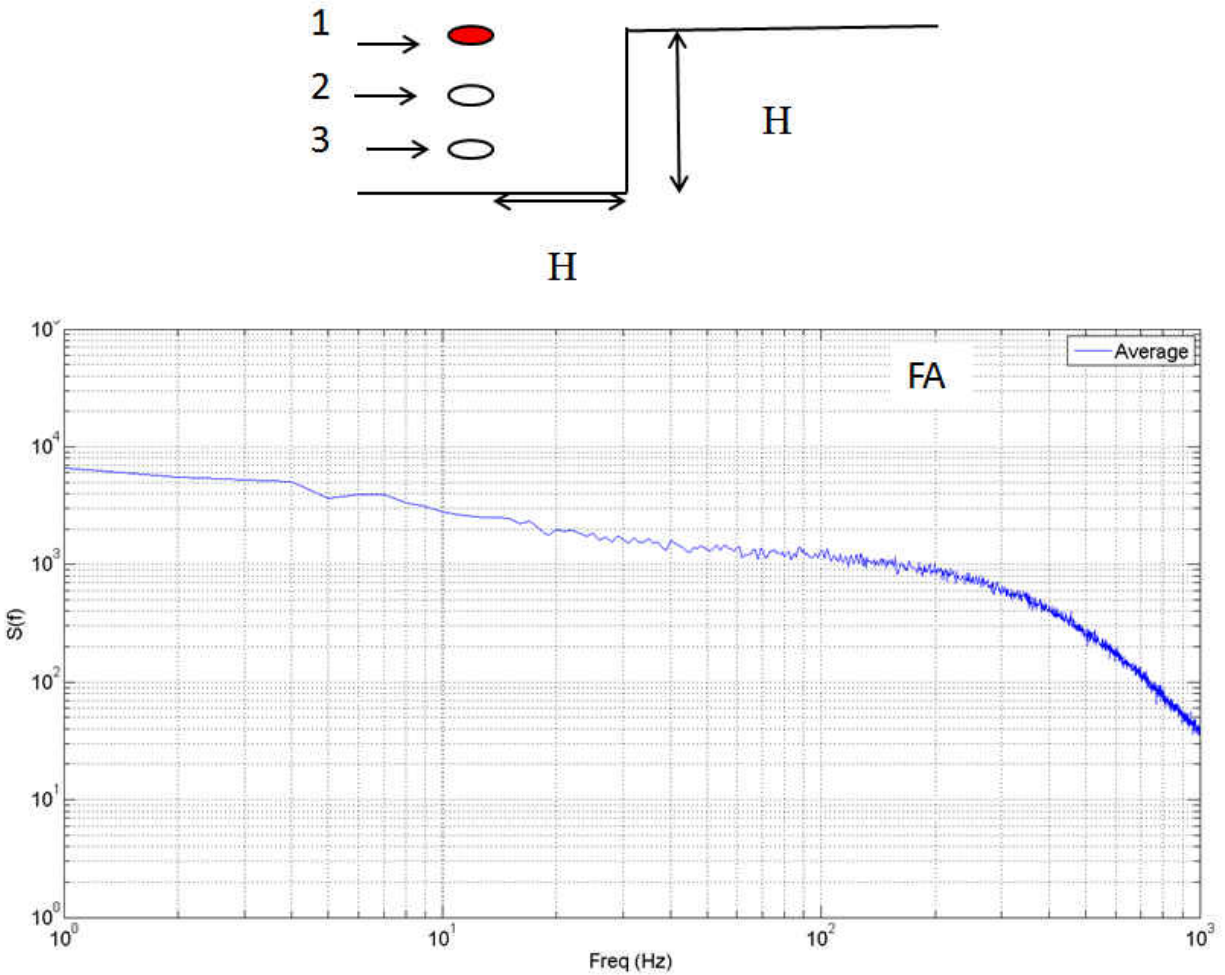


Figure 49: FFT for backward facing step shear layer FA case

A likely candidate for flow unsteadiness is the c-stage ring located in the combustor portal inlet. This geometry closely resembles a cylinder in cross flow. The FFT was taken for a signal measured at approximately 30° in the combustor portal and 5 c-stage diameters downstream for the cylinder for the FA case. This signal is presented in Figure 50. Unfortunately no distinct frequencies are detected in this location. This could be a result of the swirl velocity in the combustor portal and the inability of the single component probe to measure it adequately. The LDV system will be used in the next phase to confirm this finding.

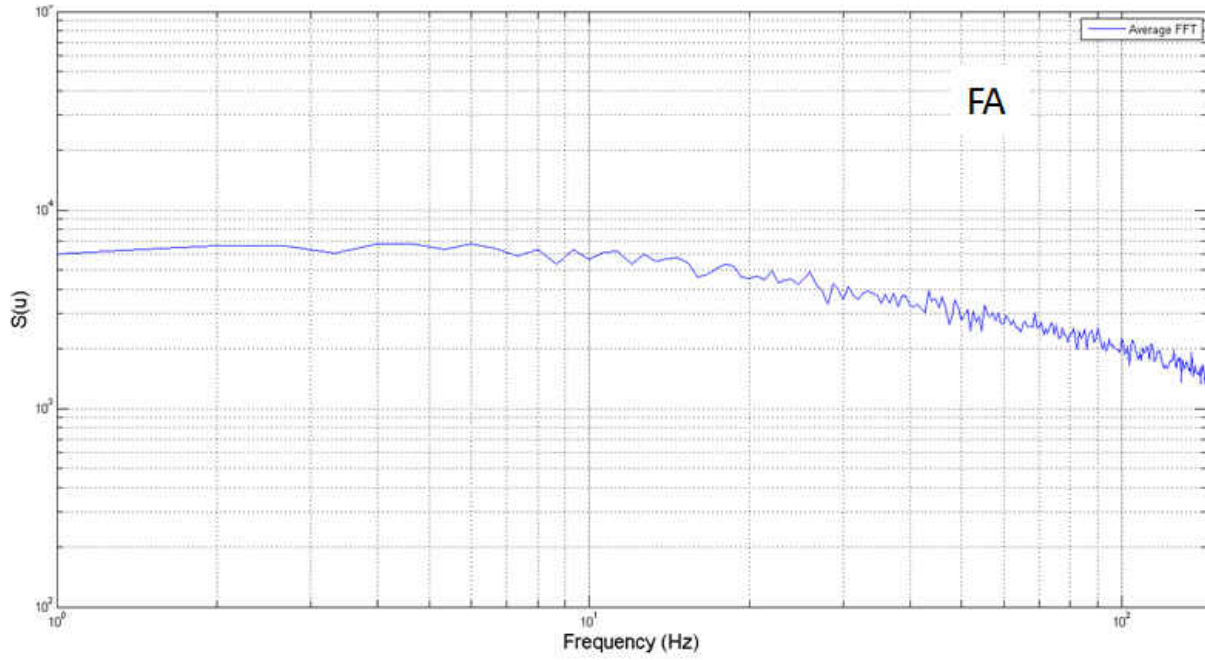


Figure 50: FFT for the c-stage cylinder for the FA case

Steady Numerical Results

The steady RANS results provide many useful measures of comparison with the steady experimental work presented thus far. Efforts were made to “instrument” the CFD following the experimental methods where available. First, a look at the centerline mean velocity magnitudes for the two different inlet conditions. This comparison is shown in Figure 51. In the CED region of the SB case, the flow separation can be seen at about 60% of the CED bottom wall length. This separation location agrees with the experimental value according to tuft visualizations. Behind the wake region of the CED strut the flow turns upward towards the transition piece. Here the flow splits around the transition and exits the centerline plane. Most of the other regions are low velocity recirculation regions. The FA case mid height velocity deficit from the screens at the inlet is carried through the entire CED. This effect is not seen in the experimental case as the velocity profile diffuses more rapidly than is predicted using the RKE RANS model. Nevertheless, the flow remains attached throughout the diffuser as is observed in the experiments. The flow turns upward at a slightly lower angle than the SB case, before impinging on the transition. When looking at the near wall velocity contours for each case in Figure 52, several observations are apparent which are not directly measureable in the experiments. For the SB case, the flow separates much earlier than the centerline due to the wall effects near the corners of the CED. The deflector plate on the bottom wall of the MidFrame cavity appears to have some impact on the acceleration of the flow as it turns towards the transition. The acceleration (‘Venturi effect’) between the side wall and transition is apparent in this plane. This effect is seen even in 360° models and at engine conditions as shown by the work of Agrawal et

al. The flow makes another turn towards the combustor portal. Some of the flow tends towards bottom dead center (BDC) of the combustor portal to fill the void at this location. The FA case has a similar trend, though it appears there is less flow tending toward BDC.

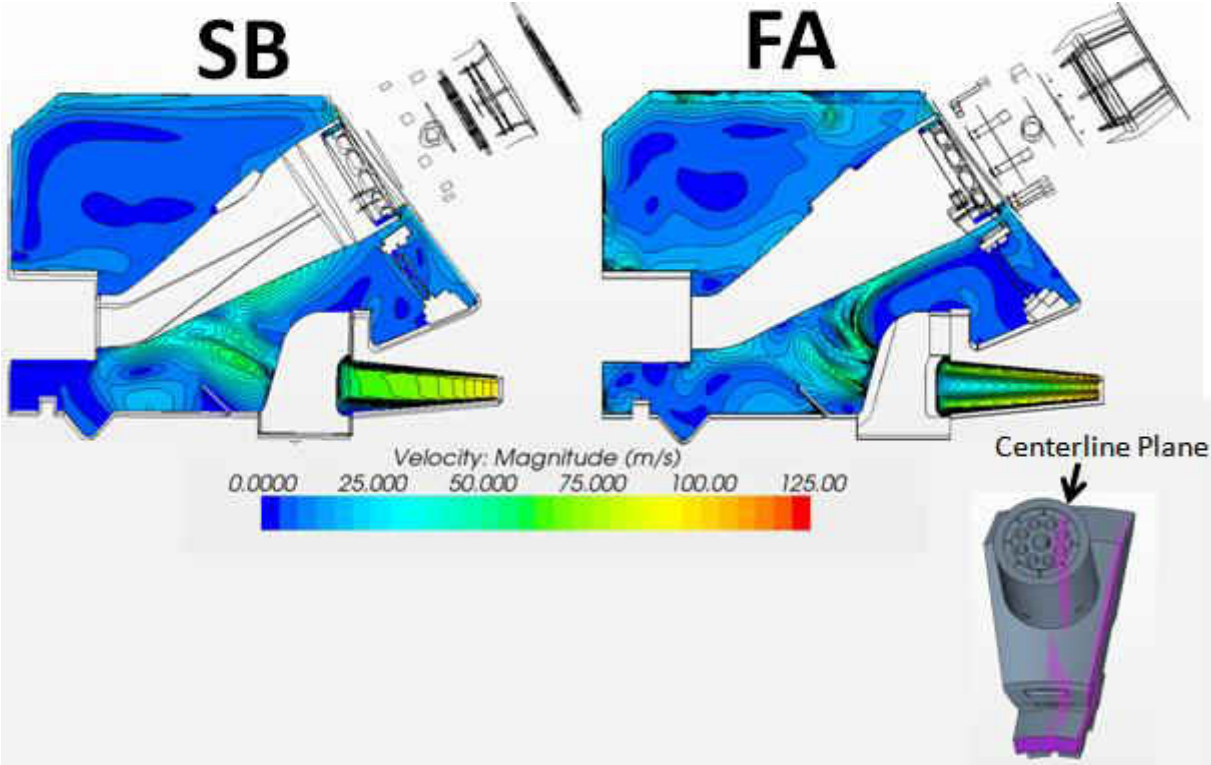


Figure 51: Comparison between centerline mean flow for the two inlet conditions

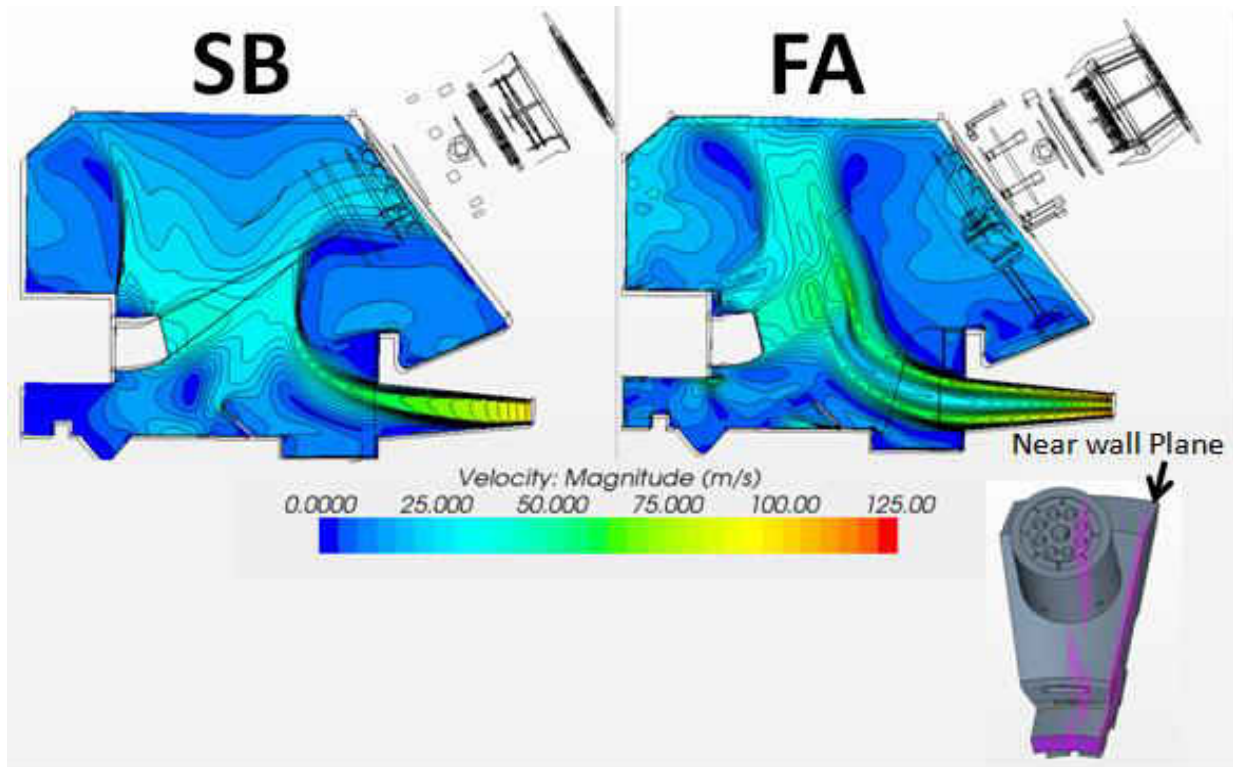


Figure 52: Comparison between near wall flow for the two inlet cases

The comparison of CED C_p with experimental values is shown in Figure 53. In general the CFD is over predicting the C_p in both cases, much more so for the SB case. The experiment showed a maximum C_p of about 0.35 while the CFD SB case is nearly double that at 0.65. The FA case is over predicted by about 5% for the FA case. The fact that the experimental FA case and CFD SB case overlap is coincidental. This discrepancy in CFD values may be due to CFD post processing techniques as the points were aligned through the center of the duct for CFD, but were taken from wall static taps in the experiments. This impact should not be drastic since the static pressure over the flow cross section should not vary significantly from experimental measurements.

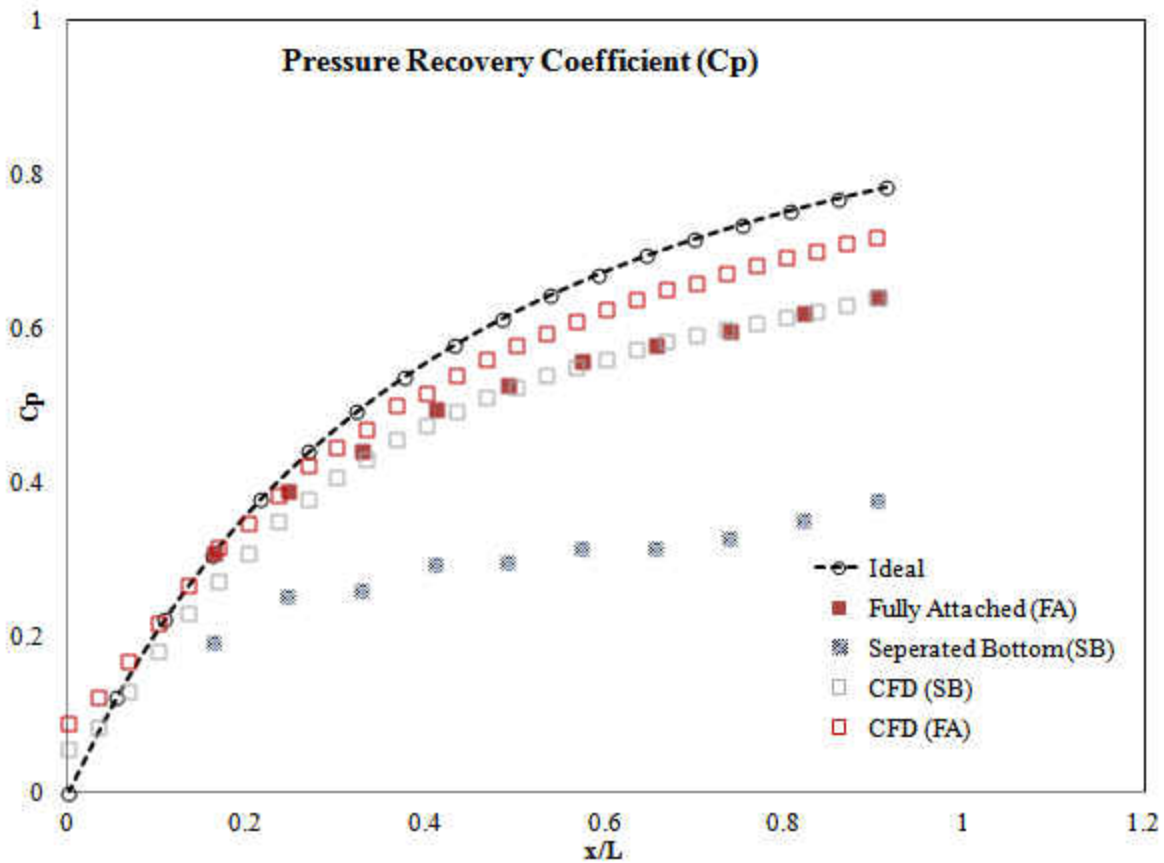


Figure 53: Cp Plot comparison with experimental and CFD predictions

Top hat point probes were positioned corresponding to the Kiel probe heads used in the experiment. Total pressure profiles are plotted for the two CFD cases in Figure 54. The lower total pressure at 135° is due to the wake region behind the mounting support for the C-stage ring. In general the flow is non uniform for both cases. Figure 55 shows the axial velocity profile at the same location. There is no measure of these values for the experimental case due to access issues with Pitot-static probes, only total pressures can be measured in the experiment. The axial velocities are also non-uniform.

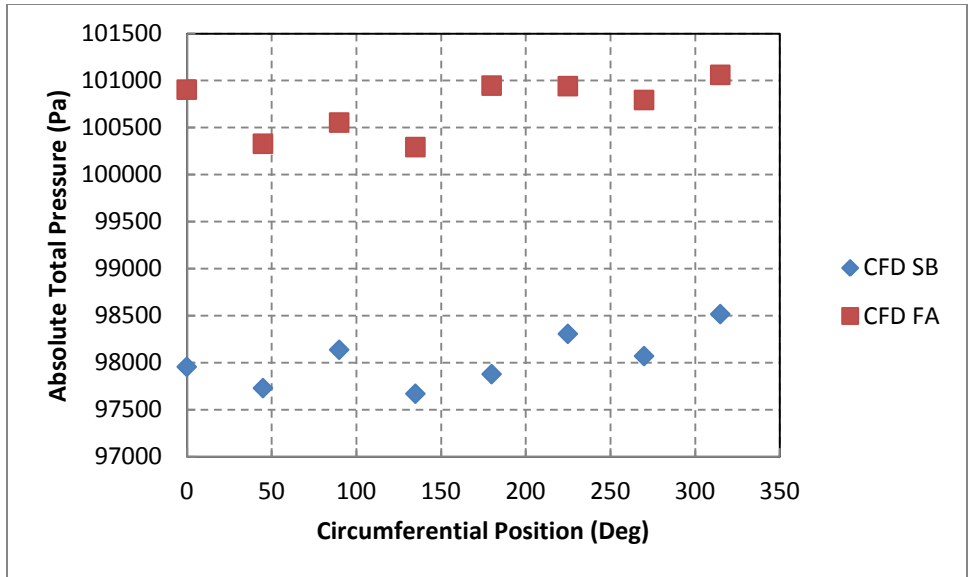


Figure 54: Comparison of top hat region total pressure profiles for CFD cases

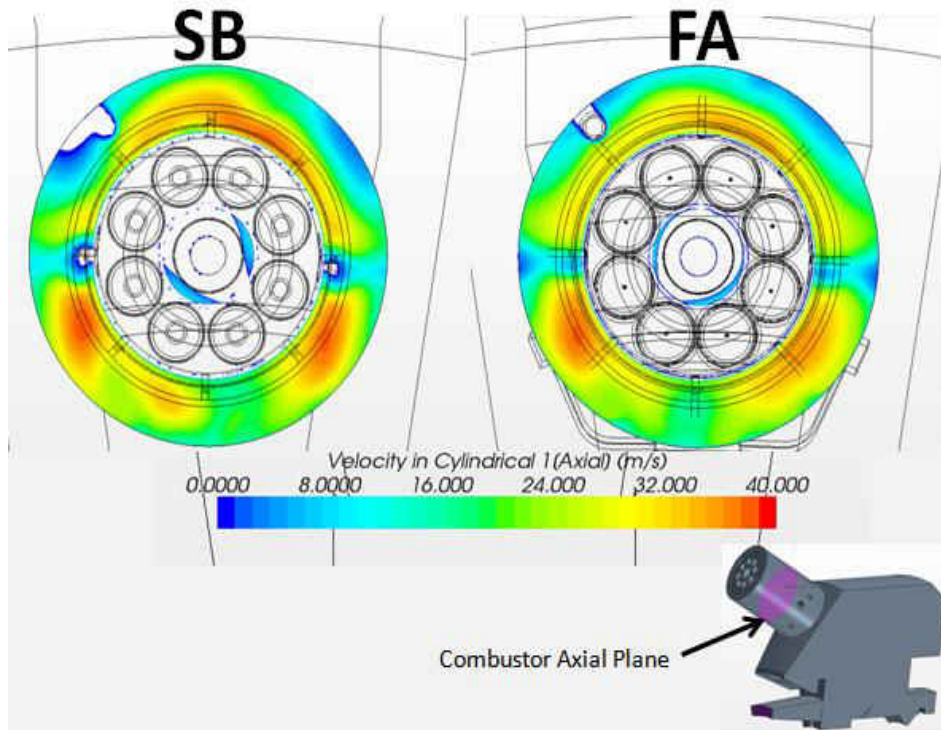


Figure 55: Comparison of top hat region axial profiles for CFD cases

The total pressure loss is presented in two forms. The first is normalized by the inlet dynamic head and presented as a percentage. The second is normalized by the inlet total pressure and also presented as a percentage. Table 3 presents these values as well as the CED max Cp for each CFD case. Also shown in Figure 56 is the total pressure loss coefficient which is a spatial representation of where the majority of losses are occurring. The SB case shows nearly 2% pressure drop in the separation region of the CED. The FA case has about 1% in the shear layer of the non-uniform velocity profile. The FA case has lower values leading into the combustor portal.

Table 3: Summary of CFD cases

Case	Pressure Drop (%Pt_in)	Pressure Drop (%Pdyn)	CED Cp
SB	2.96	51	0.64
FA	2.8	40	0.72

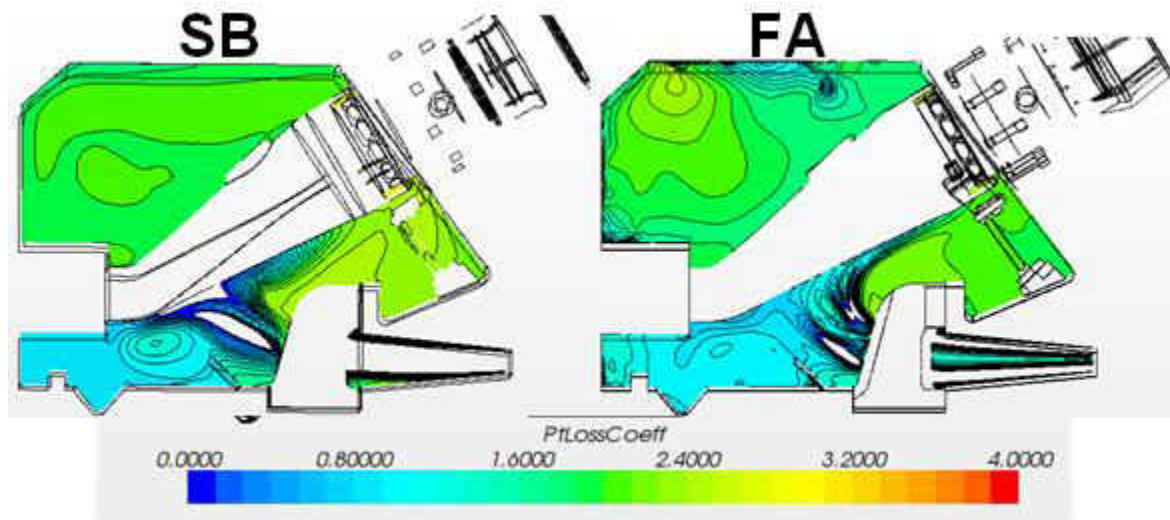


Figure 56: Total Pressure loss coefficient comparison

CONCLUSIONS

The goals of this work were to develop distinct inlet conditions and quantify the impact of the CED performance on the mean and time varying flow structures. The inlet conditions were designated as a separated bottom wall CED and a fully attached CED as two extreme cases. Previous studies on the efficacy of screens for inducing skewed velocity profiles were used to achieve the fully attached CED inlet condition. The impact of the inlet conditions was evaluated throughout the domain but with particular attention to the combustor portal and flow structures generated upstream where the flow most influences the combustion process.

The mean CED performance was drastically altered by the different inlet velocity profiles as evidenced by the microtuft visualization and pressure measurements. The increased performance of the CED which feeds the rest of the MidFrame cavity can be seen to increase the pressure coefficient of the rest of the MidFrame cavity. The trends are very similar with slightly increased range of pressure coefficient for the SB case which has a higher velocity (and smaller) jet from the CED. A correlation for inlet mass flow was developed using the automated CED inlet velocity traverse and a single point at the exit of the transition. This was developed to ensure a constant Mach number and mass flow parameter between inlet cases. Combustor portal static pressures showed similar trends of increasing pressure coefficient moving toward the combustor inlet with slightly higher flows rates in the bottom portion near the 180° location. Combustor portal average total pressures were similar for both inlet cases. The circumferential variation was minimal for both separated and attached CED conditions. A methodology was developed for reducing the number of frequencies for the first investigations on prominent unsteadiness in the MidFrame to avoid the overwhelming number of frequencies detected in the

static pressure microphone signals. The locations were sampled simultaneously with adjacent wall mounted accelerometers to identify potential fluid-wall coupled oscillations which are deferred for future investigations. Several peaks remained after this elimination process and were targeted using coherence between multiple location simultaneous microphone sampling. Once targeted, Strouhal numbers from literature for simple geometries are used to predict a range of possible frequencies of suspected geometries. Attempts were made at validating the unsteadiness with a single component thermal anemometry system. The limited access and complicated flow angles proved difficult for validating even the simplest suspected geometries. The CED inlet condition appears to have an impact on the frequencies generated downstream with possible impacts on pressure loss and combustion.

APPENDIX: DETAILED UNCERTAINTY CALCULATIONS

CED Velocity Probe Uncertainty

Typical Values:

$$V = \sqrt{\frac{2 \cdot P_{\text{dyn}}}{\rho}}$$

$$R := 287 \frac{\text{J}}{\text{kg} \cdot \text{K}} \quad T := 303 \text{K} \quad P := 101325 \text{Pa}$$
$$P_{\text{dyn}} := 8000 \text{Pa} \quad \rho := 1.15 \frac{\text{kg}}{\text{m}^3}$$
$$P_s := 3500 \text{Pa} \quad P_t := 8000 \text{Pa}$$

Density $\rho = \frac{P}{R \cdot T}$

Pressure $u_p := 100 \text{Pa}$
 $d\rho_p := \frac{1}{R \cdot T}$

Temperature $u_T := 1 \text{K}$
 $d\rho_T := \frac{-P}{R \cdot T^2}$

$$u_\rho := \sqrt{u_p^2 \cdot d\rho_p^2 + u_T^2 \cdot d\rho_T^2} \quad u_\rho = 4.014 \times 10^{-3} \frac{\text{kg}}{\text{m}^3}$$

Dynamic Pressure

$$u_{p_d} := 10000 \text{Pa} \cdot 0.001 = 10 \text{Pa} \quad \text{Full scale range of transducer (HCXM050D6H)}$$
$$2.50 \cdot 10^{-3} \text{bar} = 1 \times 10^4 \text{Pa}$$

Rated uncertainty 0.1% FSR

Velocity

$$u_{p_d} := 10 \text{Pa}$$

$$dV_{p_d} := 0.5 \cdot \left(\frac{2 \cdot P_{\text{dyn}}}{\rho} \right)^{-0.5} \cdot \frac{2}{\rho}$$

$$u_\rho = 4.014 \times 10^{-3} \frac{\text{kg}}{\text{m}^3}$$

$$dV_\rho := 0.5 \cdot \left(\frac{2 \cdot P_{\text{dyn}}}{\rho} \right)^{-0.5} \cdot \frac{-2 \cdot P_{\text{dyn}}}{\rho^2}$$

$$u_V := \sqrt{u_{p_d}^2 \cdot dV_{p_d}^2 + u_\rho^2 \cdot dV_\rho^2} \quad u_V = 0.219 \frac{\text{m}}{\text{s}} \quad \frac{0.219}{90} \cdot 100 = 0.24\%$$

or 3% of dynamic pressure due to angle $0.03 \cdot P_{\text{dyn}} = 240 \text{Pa}$ then $u.V = 1.78 \text{m/s}$ or 2%

Sidewall Static Pressures

FSR is 20 inches water = 20*249Pa = 20*249Pa = 4.98×10^3 Pa

12 bit DAQ resolution $\frac{1}{4096} = 2.441 \times 10^{-4}$

$$\frac{5000\text{Pa}}{2^{12} - 1} = 1.221 \text{ Pa}$$

$$u_{p_s} := 1.2\text{Pa}$$

or 0.1% FSR

$$u_{p_s} := 0.001 \cdot 10000\text{Pa}$$

$$u_{p_s} = 10\text{ Pa} \quad \frac{10}{3500} \cdot 100 = 0.286 \%$$

Total Pressure

Using same transducer as static pressures, calibration shows no uncertainty within +45 degrees

$$u_{p_t} := 10\text{Pa} \quad \frac{10}{8000} \cdot 100 = 0.125 \%$$

Microphone Pressure

Rated as +/- 0.2 dB

$$u_{p_{mic}} := 1\text{atm} \cdot 10^{0.02} - 1\text{atm} \quad 10^{0.02} = 1.047$$

$$u_{p_{mic}} = 4.775 \times 10^3 \text{ Pa}$$

10 V FSR sensitivity of 50 mV/Pa $\frac{10}{0.05} = 200$ Pa Unsteady fluctuation range

0.2 dB at $P_0 = 101325\text{Pa}$

$$u_{p_{mic}} := 1.5\text{Pa} \quad \frac{1.5}{200} \cdot 100 = 0.75 \%$$

Accelerometer

12 bit output at FSR of 2 g

$$u_a := \frac{2.9.81 \frac{\text{m}}{\text{s}^2}}{2^{12} - 1}$$

$$u_a = 4.791 \times 10^{-3} \frac{\text{m}}{\text{s}^2} \quad \frac{0.005}{2.9.81} \cdot 100 = 0.025 \%$$

Uncertainty in Sampling Time

smallest time between samples =

$$f = \frac{1}{T}$$

$$df_f := \frac{-1}{T^2} = -3.6 \times 10^7 \frac{1}{\text{s}^2}$$

$$u_f := \sqrt{u_T^2 \cdot df_f^2}$$

$$u_f = 9 \frac{1}{\text{s}}$$

$$u_T := \frac{1}{2 \cdot 10^6} \cdot 0.5 \text{s} \quad \text{half the resolution}$$

$$T := \frac{1}{6000} \text{s} \quad \text{typical time period}$$

REFERENCES

- Agrawal, A. K., Kapat, J. S., Yang, T. T., 1998, "An Experimental Computational Study of Airflow in the Combustor-Diffuser System of a Gas Turbine for Power Generation", *Journal of Engineering for Gas Turbines and Power*, Vol. 120, pp. 24-33.
- Boyce, M., 2006, "Gas Turbine Engineering Handbook", Gulf Professional Publishing.
- Carrotte, J. F., Denman, P. A., Wray, A. P., Fry, P., 1994, "Detailed Performance Comparison of a Dump and Short Faired Combustor Diffuser System", *Journal of Engineering for Gas Turbines and Power*, Vol. 116, pp. 517-526.
- Cengel, Y.A., and Boles, M.A., 2006, "Thermodynamics: an engineering approach," McGraw-Hill Higher Education New York
- Cherry, E. M., Elkins, C. J., Eaton, J. K., 2008, "Geometric Sensitivity of Three-Dimensional Separated Flows", *International Journal of Heat and Fluid Flow*, Vol. 29, pp. 803-811.
- Durbin, P. A., 1996, "On the k-3 Stagnation Point Anomaly", *International Journal of Heat and Fluid Flow*, Vol. 17, pp. 89-90.
- Higman, C., and Van der Burgt, M., 2003, "Gasification," Gulf Professional Publishing.
- Karki, K. C., Oechsle, V. L., Mongia, H. C., 1992, "A Computational Procedure for Diffuser-Combustor Flow Interaction Analysis", *Journal of Engineering for Gas Turbines and Power*, Vol. 114, pp. 1-7.
- Ke, F., Liu, Y. Z., Wang, W. Z., Chen, H. P., 2006, "Wall Pressure Fluctuations of Turbulent Flow over Backwards-Facing Step with and without Entrainment: Microphone Array Measurement", *Journal of Hydrodynamics*, Vol. 18, pp. 393-396.
- Kibicho, K., Suyaers, A. T., 2008, "Measurements of Velocity Profiles and Static Pressure Recovery in a Wide-Angled Diffuser", *R & D Journal of the South African Institution of Mechanical Engineering*, Vol. 24, pp. 16-22.
- Lefebvre, A.H., 1999, "Gas Turbine Combustion," CRC.
- Liu, Y. Z., Ke, F., Wang, W. Z., Cao, Z. M., 2006, "Pressure-Velocity Joint Measurements of a Wall-Bounded Turbulent Shear Flow", *Journal of Hydrodynamics*, Vol. 18, pp. 315-318.
- Liu, Y. Z., Ke, F., Sung, H. J., 2008, "Unsteady Separated and Reattaching Turbulent Flow Over a Two-Dimensional Square Rib", *Journal of Fluids and Structures*, Vol. 24, pp. 366-381.

- Mahalakshmi, N. V., Krithiga, G., Sandhya, Vikraman, J., Ganesan, V., 2007, "Experimental Investigations of Flow Through Conical Diffusers with and without Wake Type Velocity Distortions at Inlet", *Experimental Thermal and Fluid Science*, Vol. 32, pp. 133-157.
- Mehta, R. D., Bradshaw, P., 1979, "Design Rules for Low Speed Wind Tunnels", *The Aeronautical Journal of the Royal Aeronautical Society*, pp. 444-449.
- Orth, U., Ebbing, H., Krain, H., Weber, A., Hoffman, B., 2002, "Improved Compressor Exit Diffuser for an Industrial Gas Turbine", *Journal of Turbomachinery*, Vol. 124, pp. 19-26.
- Walker, A. D., Denman, P. A., McGuirk, J. J., 2004, "Experimental and Computational Study of Hybrid Diffusers for Gas Turbine Combustors", *Journal of Engineering for Gas Turbines and Power*, vol. 126, pp. 717-725.
- Zhang, Q. S., Liu, Y. Z., 2012, "Wall-Pressure Fluctuations of Separated and reattaching Flow over Blunt Plate with Chord-to-Thickness Ratio $c/d = 9.0$ ", *Experimental Thermal and Fluid Science*, Vol. 42, pp. 125-135.